JGR Planets

RESEARCH ARTICLE
10.1029/2025JE009475

A Long-Lived Vortex From Saturn's 2010 Giant Convective Storm

Xinyue Wang[1,2], Liming Li[3], Xun Jiang[2], Cheng Li[1], Salma Noor[2], Julissa M. Rivas[2], Patrick M. Fry[4], Amy A. Simon[5], Raúl Morales-Juberías[6], Agustin Sánchez-Lavega[7], Enrique García-Melendo[8], Aida Flix Bellmunt[8], Michael H. Wong[9], Ulyana A. Dyudina[10], and Trevor Barry[11]

[1]University of Michigan, Ann Arbor, MI, USA, [2]Department of EAS, University of Houston, Houston, TX, USA, [3]Department of Physics, University of Houston, Houston, TX, USA, [4]University of Wisconsin-Madison, Madison, WI, USA, [5]NASA Goddard Space Flight Center, Greenbelt, MD, USA, [6]Physics Department, New Mexico Institute of Mining and Technology, Socorro, NM, USA, [7]Escuela de Ingeniería de Bilbao, Universidad del País Vasco, UPV/EHU, Bilbao, Spain, [8]Universitat Politècnica de Catalunya UPC, Terrasa, Spain, [9]Center for Integrative Planetary Science, UC Berkeley, Berkeley, CA, USA, [10]Space Science Institute, Boulder, CO, USA, [11]Broken Hill Observatory, Broken Hill, NSW, Australia

Key Points:

- The first complete timeline for the origin of a large vortex from a major convective storm in the atmospheres of giant planets is provided
- Key features of the vortex, including large vertical extent (>250 km) and development into a stable zonal velocity (5–10 m/s), are revealed
- The vortex has evolved into a compact and center-symmetric structure with weak beta-drift, suggesting that it may become a long-lived feature

Supporting Information:

Supporting Information may be found in the online version of this article.

Correspondence to:

L. Li,
lli7@central.uh.edu

Citation:

Wang, X., Li, L., Jiang, X., Li, C., Noor, S., Rivas, J. M., et al. (2026). A long-lived vortex from Saturn's 2010 giant convective storm. *Journal of Geophysical Research: Planets*, *131*, e2025JE009475. https://doi.org/10.1029/2025JE009475

Received 2 OCT 2025
Accepted 30 APR 2026

Abstract The giant convective storm that erupted at the end of 2010 generated a large vortex. In this study, we systematically examine this vortex using long-term multi-wavelength observations from the Cassini spacecraft and the Hubble Space Telescope. Our analysis reveals that the vortex has persisted for more than 14 years. It has evolved into a compact and center-symmetric structure with a vertical extent of at least 250 km. A vorticity-gradient analysis indicates that the beta-drift effect contributes to its meridional motion, while its zonal velocity is primarily controlled by the background large-scale winds. Stability analysis further suggests that the vortex has migrated to a relatively stable latitudinal band. Together, these findings suggest that the vortex has entered a stable state and may persist for an extended period, with the potential to become a long-lived feature in Saturn's atmosphere. These observations provide the first complete timeline for the origin of a large and long-lived anticyclonic vortex produced by a major convective storm in the atmospheres of giant planets. This observational study not only improves our understanding of Saturn's vortex systems but also offers critical constraints for developing theoretical and numerical models of vortex dynamics in planetary atmospheres.

Plain Language Summary In late 2010, a giant convective storm erupted in Saturn's atmosphere, generating a massive swirling vortex, similar to a gigantic midlatitude anticyclone on Earth but far larger and longer lasting. Using more than a decade of observations from Cassini spacecraft and the Hubble Space Telescope, we tracked this vortex and discovered that it has survived for over 14 years. Our study shows that the vortex began as a relatively convective structure and gradually evolved into a more organized state. The vortex also developed a large vertical extent stretching over 250 km. We found that its movement is shaped by Saturn's background winds and vorticity field. Finally, stability analysis suggests the vortex has become stable and potentially long-lived in Saturn's atmosphere. This study provides the first complete timeline for the origin of a large and long-lived vortex produced by a major convective storm in the atmospheres of giant planets. It gives scientists a rare and detailed view of how giant storms on gas planets can create long-lasting weather features. It also improves our understanding of how atmospheric vortices form, evolve, and persist not only on Saturn but also on other planets across our solar system.

1. Introduction

Vortices are fundamental features of atmospheric systems on rotating planets, arising from the Coriolis effect induced by planetary rotation (e.g., Holton & Hakim, 2013; Wallace & Hobbs, 2006). They play a central role in shaping planetary weather and climate. On Earth, vortical systems such as tropical cyclones, mid-latitude cyclones, anticyclones, and polar vortices are key agents in redistributing air masses, chemical species, momentum, and energy. Consequently, these vortices influence both short-term weather events and long-term climate variability (e.g., Emanuel, 1991, 2003; Held & Hou, 1980; Hoskins & Hodges, 2002; Waugh & Randel, 1999). In addition, vortices in planetary atmospheres serve as natural laboratories for testing theories of geophysical fluid dynamics under different planetary conditions.

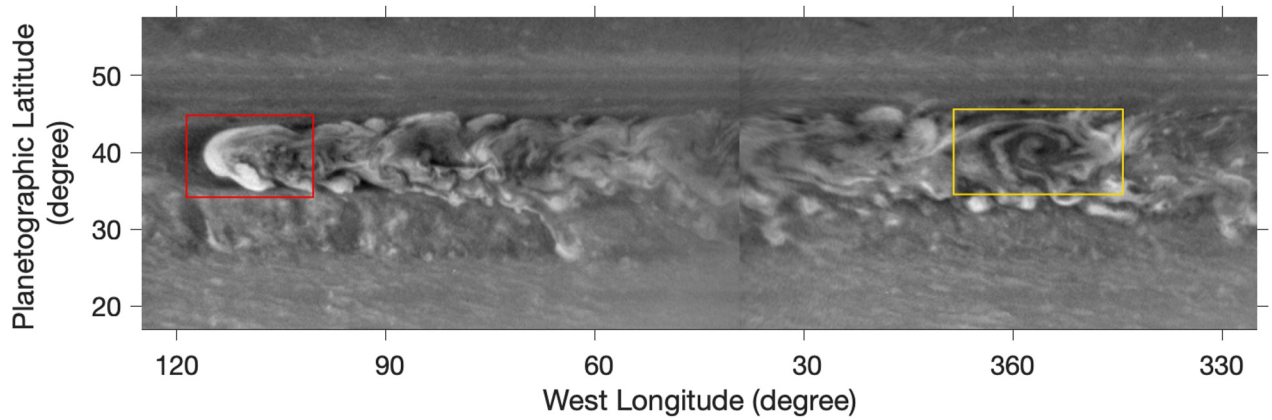

Figure 1. Overview of Saturn's 2010 giant convective storm highlighting the large anticyclonic vortex (AV) generated by the storm. The map is constructed from raw Imaging Science Subsystem images obtained using the second continuum filter (CB2, ~752 nm). The two images used to generate the map were recorded on 25 February 2011 with spatial resolutions of 136 km/pixel (~0.14 degrees/pixel) and 140 km/pixel (~0.15 degrees/pixel), respectively. Because the conversion between km/pixel and degrees/pixel depends on latitude and viewing direction (longitudinal versus latitudinal), the values reported here represent averages over the relevant latitudes and directions. The storm head and the AV are highlighted by red and yellow rectangles, respectively.

Beyond Earth, vortices are ubiquitous in the atmospheres of gas giant planets. The vortices on Jupiter and Saturn exhibit scales, lifetimes, and dynamical regimes distinct from those on Earth. Large-scale vortices such as Jupiter's Great Red Spot (GRS) and polar vortices (e.g., Adriani et al., 2018; Dowling & Ingersoll, 1989; Dyudina et al., 2008; Fletcher et al., 2018; Ingersoll et al., 2004; Marcus, 1993; Sánchez-Lavega et al., 2024; Sayanagi et al., 2018; Simon et al., 2018; Wong et al., 2021) play essential roles in shaping the large-scale circulation and interacting with other weather systems. Their longevity and vast size make them valuable tracers of atmospheric stability, vertical structure, and chemical composition over timescales ranging from years to centuries.

The number of long-lived vortices on Saturn is very limited, and the corresponding studies are relatively few (e.g., García-Melendo et al., 2007; del Río-Gaztelurrutia et al., 2018). A long-lived anticyclone located at 76°N, known as the North Polar Spot, was discovered and studied using Voyager and HST observations (Sánchez-Lavega et al., 1993, 1997). However, long-lived vortices originating from convective storms had not been reported prior to the Cassini era. An important opportunity arose with the giant convective storm that erupted in December 2010, observed by the Cassini spacecraft and ground-based telescopes (e.g., Fischer et al., 2011; Fletcher, Baines, et al., 2011; Fletcher, Hesman, et al., 2011; Sánchez-Lavega et al., 2011). This storm generated several vortices (e.g., García-Melendo & Sánchez-Lavega, 2017; Sánchez-Lavega et al., 2012; Sayanagi et al., 2013). Among these vortices, the largest appears to have an unusually long lifetime, much longer than that of many other mid-latitude vortices, whose lifetimes are typically less than one Earth year (e.g., Trammell et al., 2016).

Figure 1 shows the giant storm, including the largest vortex formed in its aftermath. The vortex, located within the developed stream of the storm head, evolved into an oval-shaped structure by January 2011, about one month after the storm's onset. Previous studies (e.g., García-Melendo et al., 2013; Sayanagi et al., 2013) suggest that the vortex is an anticyclone. In this study, we refer to the vortex as the Anticyclone Vortex (AV), following the nomenclature provided in a previous study (Hueso et al., 2020). Remarkably, the AV has persisted for more than a decade (2011-present), surviving through more than one Saturnian season and remaining detectable in recent observations. Although long-lived vortices have been discovered on Jupiter, Saturn, and Neptune (Baines et al., 2019; Dowling & Ingersoll, 1989; García-Melendo et al., 2007; Marcus, 1993; Sánchez-Lavega et al., 1993, 1997; Sromovsky et al., 2001, 2002; Wong et al., 2019), the formation of most of these vortices has not been directly observed. Fortunately, the formation of the long-lived AV following Saturn's 2010 giant storm was observed by both ground-based observatories and the Cassini spacecraft (Fischer et al., 2011; Fletcher, Baines, et al., 2011; Fletcher, Hesman, et al., 2011; Sánchez-Lavega et al., 2011). Long-term observations of the AV since its formation therefore provide an exceptional case to study vortex dynamics on Saturn.

In this work, we take advantage of extensive observations spanning more than a decade by combining long-term multi-wavelength data sets from Cassini (2010–2017) and HST (2018–2025). These complementary data sets

enable a systematic investigation of the AV's morphology, drift rate, vertical cloud structure, and spectral properties. By tracing its evolution across atmospheric layers and over many years, we aim to establish the fundamental characteristics of Saturn's large vortices. Furthermore, comparative studies between Saturn and other planets may provide a broader perspective for understanding vortex dynamics as a general phenomenon in planetary atmospheres.

2. Observations and Data Processing

2.1. Cassini Observations

The Cassini spacecraft was an international planetary mission dedicated to exploring the Saturn system (e.g., Jaffe & Herrell, 1997). During its 14-year tour of Saturn (2004–2017), Cassini observed the eruption of a giant convective storm in 2010 and monitored its evolution until the end of the mission. In this study, we analyze observations from two Cassini instruments: the Imaging Science Subsystem (ISS) (Porco et al., 2004) and the Visual and Infrared Mapping Spectrometer (VIMS) (Brown et al., 2004).

The ISS is a two-dimensional imaging system consisting of two framing cameras: a narrow-angle camera with a 0.35° square field of view (FOV) and a wide-angle camera with a 3.5° square FOV (Porco et al., 2004). In this work, we primarily use images from the wide-angle camera because its larger FOV provides a more frequent coverage of the AV. ISS includes more than 12 spectral filters. Here we focus mainly on images obtained with the continuum filter CB2 (752 nm), which senses the top visible cloud deck (ammonia clouds) and has been widely used to study Saturn's zonal winds and cloud morphology (Porco et al., 2005; Sánchez-Lavega et al., 2006, 2007; Sayanagi et al., 2013; Vasavada et al., 2006). We also analyze images taken with the methane-absorption filter MT3 (890 nm), which probes stratospheric hazes above the visible clouds and helps constrain the vertical structure of the AV.

By searching the complete ISS data set on the Planetary Data System (PDS), we identified 183 CB2 images containing the AV between 2010 and 2016. We did not find any ISS images capturing the AV in 2017, likely due to the special observing strategy of the Grand Finale phase, which prioritized high-resolution regional observations. We also found 128 MT3 images containing the AV. These selected images were processed with the Integrated Software for Imagers and Spectrometers (ISIS) (Gaddis et al., 1997) developed by the U.S. Geological Survey (https://isis.astrogeology.usgs.gov/). The data processing involved three main steps: photometric calibration, navigation, and map projection. Photometric calibration followed the latest version of the Cassini ISS calibration software (Knowles et al., 2020; West et al., 2010). Image navigation used the camera geometric model together with the Navigation and Ancillary Information Facility (NAIF) toolkit (Vasavada et al., 2006). The images were then projected onto cylindrical maps, which are appropriate for the AV located at Saturn's mid-latitudes. These procedures are standard and have been described in detail in our previous studies (L. Li et al., 2004, 2006, 2011, 2018, 2021, 2023).

The regional maps processed from the CB2 images are used to examine the temporal evolution and drift in both latitude and longitude of the vortex, and the MT3 images are mainly utilized to examine the vertical structure of the vortex. Among the 183 CB2 regional maps including the AV, many were recorded in groups with short time intervals ranging from ∼10 min to ∼1 hr. Over such short intervals, the AV showed little change in size and location, and navigation errors were often larger than any actual changes. For these groups, we selected a single representative map for further analysis. With this selection criterion, 25 maps were chosen from the 183 CB2 maps. The time intervals between the selected maps ranged from ∼13 to ∼290 days.

Unlike the ISS, which is a framing camera system, the VIMS is an imaging spectrometer that provides both spatial and spectral information (Brown et al., 2004). The VIMS observed Saturn at 352 wavelengths spanning ∼351–∼5,131 nm, with spectral resolutions ranging from ∼4 to ∼25 nm. The instrument consists of two channels: the visible channel (VIS, 351–1,046 nm) and the infrared channel (IR, 892–5,131 nm). To construct continuous spectra from 351 to 5,131 nm, we follow the method of Filacchione et al. (2007), which showed that bridging the VIS and IR spectra at 980 nm provides the most reliable results. The VIMS FOV (1.83°) is smaller than that of the ISS wide-angle camera (3.5°), but the instantaneous FOV (IFOV, the spatial extent of a single spectral sample) is larger in VIMS than in ISS because of the different spatial sampling (32 or 64 pixels for VIMS compared to 256, 512, or 1,024 pixels for ISS), which is consistent with the lower spatial resolution of VIMS compared with ISS.

From the complete VIMS data set on the PDS, we identified 10 observations (cubes) containing the AV between 2011 and 2015. Among them, 8 observations have relativley high data quality. No high-quality VIMS observations capturing the AV were found during the final two years of the Cassini mission (2016–2017). The VIMS data were processed using the standard pipeline developed by the instrument team (e.g., Barnes et al., 2007; Brown et al., 2004; Sromovsky & Fry, 2010), which is implemented in ISIS. ISIS is applied to the selected VIMS cubes for calibration, navigation, and cylindrical projection (Baines et al., 2005, 2009, 2018; Brown et al., 2004; Choi et al., 2009; Gaddis et al., 1997; Sromovsky et al., 2013, 2016, 2021). The resulting VIMS maps are combined with ISS maps to investigate the AV.

2.2. HST Observations

The Cassini ISS and VIMS data provide the primary basis for analyzing the AV from the 2010 giant storm. To extend the record into the post-Cassini era, we also use HST observations to investigate the AV's long-term evolution and persistence.

The Hubble Space Telescope observations used in this study were obtained with the Wide Field Camera 3 (WFC3), which provides imaging capabilities from the ultraviolet to the near infrared (Kimble et al., 2008; Marinelli & Green, 2024). WFC3 has been extensively used for planetary observations, particularly through the Outer Planet Atmospheres Legacy (OPAL) program (Simon et al., 2015), which conducts annual monitoring of the giant planets to track atmospheric circulation, cloud morphology, and storm evolution. The OPAL observations of Saturn from 2018 to 2025 are especially important for this study because they provide continuous monitoring of the AV following the end of the Cassini mission in 2017.

The ultraviolet-visible (UVIS) channel of WFC3 has multiple filters covering wavelengths from ∼236 nm (ultraviolet) to ∼889 nm (near-infrared). The FOV of UVIS is ∼0.045°, narrower than the FOVs of Cassini ISS and VIMS. In principle, this narrow FOV allows high-resolution imaging, but in practice the great distance between the HST and Saturn limits the spatial resolution to ∼300 km/pixel. This is comparable to the worst resolution of the selected Cassini/ISS images (∼350 km/pixel) and the best resolution of the selected Cassini/VIMS images (∼240 km/pixel). Detailed descriptions of the UVIS filters and image processing are provided in Simon et al. (2015).

In this study, we mainly use processed global maps from the OPAL program, available at https://archive.stsci.edu/hlsp/opal. From these maps, we extract regional subsets containing the AV at multiple wavelengths from 2018 to 2025. The maps recorded with the F763M filter (761 nm) are used to measure the AV's size, latitude, and longitude each year. The F763M (761 nm) is close in wavelength to the Cassini/ISS CB2 (752 nm). Therefore, images from both filters (i.e., Cassini/CB2 and HST/F763M) probe the top visible clouds in the upper troposphere, enabling the tracking of the long-term evolution of the AV. For each year in the HST epoch, two global maps at F763M are available, separated by a time interval roughly corresponding to one Saturn rotation (∼10.6 hr).

In addition, we use HST global maps recorded with the F225W (236 nm), F343N (344 nm), and FQ889N (889 nm) filters to investigate the vertical structure of the AV. The F225W images sense high altitudes in the stratosphere due to strong Rayleigh scattering by gases. F343N is identical to the Cassini/ISS UV3 filter and is near the shortest wavelength of Cassini/VIMS (∼351 nm). FQ889N (889 nm) is very close to the Cassini/ISS MT3 filter (890 nm). Images recorded with F343N and FQ889N of HST/UVIS probe atmospheric layers including stratospheric hazes. The main characteristics of the Cassini and HST data sets are summarized in Table 1.

2.3. Other Observations

In addition to Cassini and HST data, ground-based telescopic observations have contributed to monitoring Saturn. These observations, often from amateur astronomers, are collected in databases such as the Planetary Virtual Observatory and Laboratory and its updated version PVOL2 (http://pvol2.ehu.eus), which are integrated into the Virtual European Solar and Planetary Access (VESPA) project (Erard et al., 2018). These data sets provide exceptional temporal coverage, complementing spacecraft observations (Hueso et al., 2020).

There are observational gaps in 2017 between the AV observations by Cassini (2011–2016) and HST (2018–2025). By examining PVOL2 global images and referring to a previous study (Hueso et al., 2020), we

Table 1
Characteristics of Cassini and HST Observations of the Vortex

Mission/Instrument	Time	Spatial resolution	Filter/Spectral characteristic
Cassini/ISS	2011–2016	~50–350 km/pixel	CB2 (752 nm) and MT3 (890 nm)
Cassini/VIMS	2011–2015	~240–1,500 km/pixel	351–5,131 nm at varying spectral resolutions (4–25 nm)
HST/WFC3	2018–2025	~300 km/pixel	F225W (236 nm), F343N (344 nm), F763M (761 nm), and FQ889N (889 nm)

confirm that the AV seen in HST images is the same one generated by the 2010 storm and captured by Cassini. These amateur observations, obtained with small telescopes, have lower spatial resolution than those from Cassini and HST. Therefore, they are not analyzed in this study except to verify the continuity of the AV.

3. Results

Based on the processed long-term multi-wavelength data sets from Cassini and HST observations, we examine the temporal evolution, dynamics, vertical structure, and spectral characteristics of the AV during the period 2010–2025.

3.1. Long-Term Evolution and Movement of the AV

Figure 2 presents maps of the large AV generated by the 2010 giant storm during 2011–2016. For each year, we select two representative maps. The images used in Figure 2 were recorded with the CB2 filter at 752 nm, a wavelength in a continuum band that primarily senses the top visible clouds (ammonia clouds) near 500–1,500 mbar in Saturn's upper troposphere (Atreya et al., 1999; Atreya & Wong, 2005; Fletcher, Baines, et al., 2011; Fletcher, Hesman, et al., 2011; Pérez-Hoyos et al., 2005, 2016; Roman et al., 2013; Simon et al., 2022; West et al., 2009). The time series in Figure 2 shows that the AV generally became smaller over time, while evolving into a more organized and compact structure. In addition to its longitudinal movement, the AV also drifted meridionally, which will be further discussed below.

Figure 3 shows maps of the AV from 2018 to 2025, derived from global maps processed by the HST/OPAL program. The HST maps at F763M and the Cassini/ISS maps at CB2 (Figure 2) both probe the top visible clouds in the upper troposphere, allowing these datasets to be combined to explore the AV's temporal evolution over an extended period. The HST maps indicate that the AV's latitude remained nearly constant except for a noticeable change between 2020 (panel c) and 2021 (panel d). The size of the AV did not change significantly during the HST observation period.

Figure 4 further examines the temporal variation using the 5000-nm images recorded by the Cassini/VIMS during the period of 2011–2015. These VIMS images probe down to the NH_4SH cloud layer (~2,000–5,000 mbar), inaccessible to ISS or HST observations. The VIMS 5000-nm images have previously been used to study the AV (e.g., Sromovsky et al., 2016), but here we conduct an extended analysis, including an examination of the temporal evolution of the AV after 2012. The time series of 5000-nm images indicates that the deep structure of the AV gradually evolved into a more organized form while shrinking in size. In addition, the AV's center shifted significantly northward during this period. These changes in the deep structure are consistent with the temporal evolution of the AV at relatively shallow atmospheric layers as observed by the ISS/CB2 images (Figure 2).

To quantitatively examine the temporal evolution the AV's size, we need to determine the boundary of the vortex. In principle, the wind field and corresponding vorticity of a vortex can be used to determine its boundary. However, for most of the AV's evolution, such measurements were not possible for two reasons: (a) the spatial resolution of most observations was insufficient, and (b) there were very few discrete cloud features within the vortex suitable for wind tracking.

From the literature, we found one study (Sayanagi et al., 2013) that measured the AV's wind and vorticity fields, based on Cassini/ISS observations of its early stage (January 2011). At that time, the AV was relatively large and contained more discrete cloud tracers. Their measurements revealed that the vortex is anticyclonic, and the vorticity measurements can be used to determine the vortex's boundary.

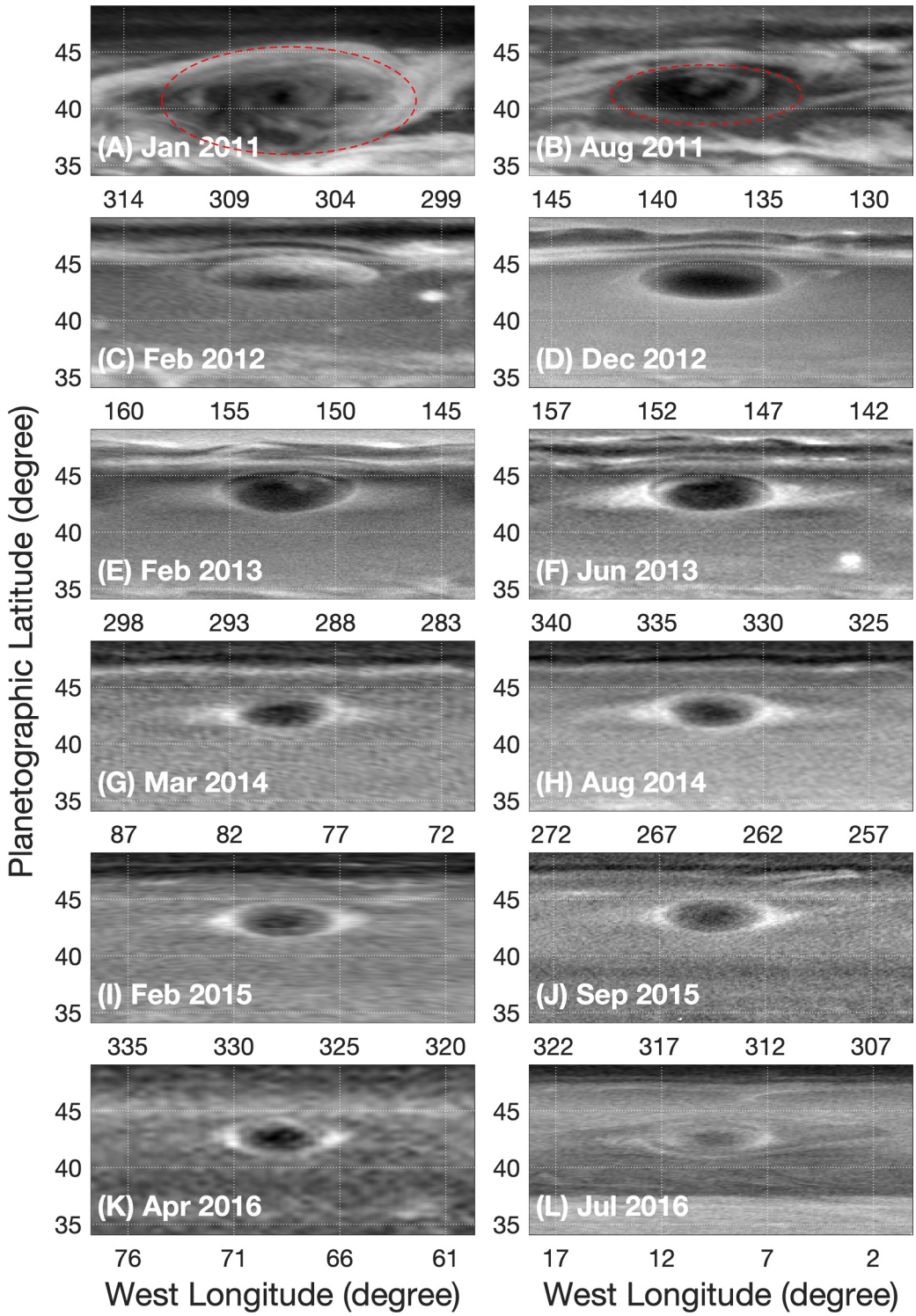

Figure 2. Time series of Imaging Science Subsystem (ISS)/CB2 maps illustrating the anticyclonic vortex's (AV's) evolution into a compact and centrally symmetric structure. In the two top panels (a) and (b), examples of the AV boundaries (mega-ellipses) are shown. Between January 2011 (panel a) and December 2012 (panel d), the AV undergoes major changes in morphology, size, and meridional position. From 2012 to 2014 (panels d–g), the vortex primarily contracts in size, and after 2014 (panels g–l) it remains largely stable in shape, size, and meridional position. Two maps are shown for each year between 2011 and 2016. The latitude range is identical in all panels to facilitate comparison of meridional drift and vortex size. Longitudes differ due to the AV's longitudinal motion but span the same range (~19 degrees) to allow comparison of longitudinal extent. The maps were constructed from ISS images taken with the CB2 filter (~752 nm) at spatial resolutions ranging from ~54 to ~345 km/pixel (~0.06–0.37 degrees/pixel). Grid lines are spaced every 5 degrees in latitude and longitude to aid identification of the AV location.

10.1029/2025JE009475

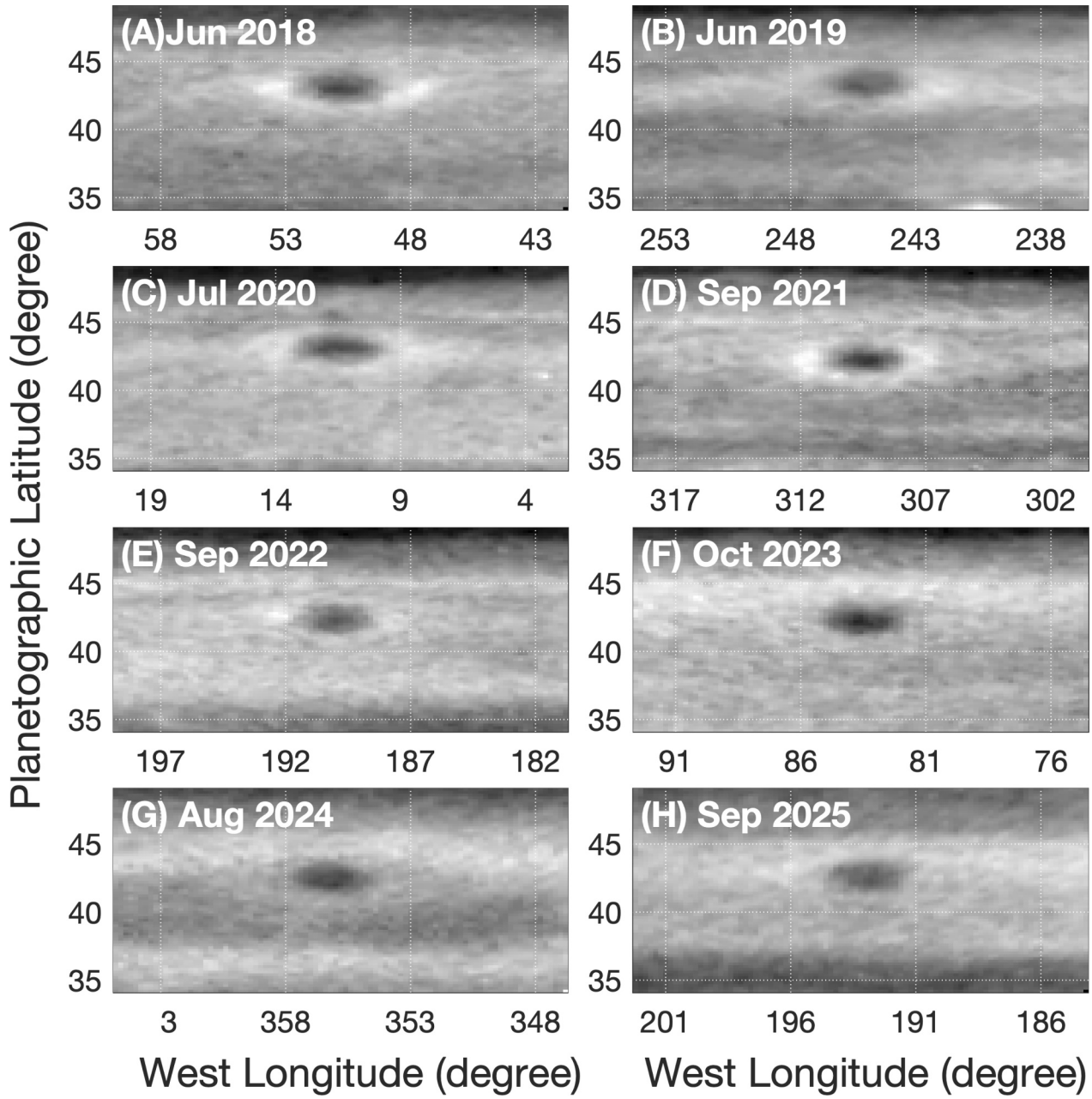

Figure 3. Time series of HST/Wide Field Camera 3 (WFC3) maps showing that the anticyclonic vortex (AV) remained basically stable from 2018 to 2025, with little change in morphology, size, or meridional position. The meridional range is identical across all panels to facilitate comparison of meridional drift and vortex size. Longitudes differ between panels due to the AV's longitudinal movement but span the same range (~19 degrees) to allow comparison of longitudinal extent. The maps were constructed from WFC3 images taken with the F763M filter (~761 nm), which is closest in wavelength to the Cassini Imaging Science Subsystem/CB2 filter (~752 nm). The spatial resolution of the WFC3 images is approximately 300 km/pixel (~0.32 degrees/pixel). Two maps separated by approximately one rotational period are available for each year of the HST epoch, but only one map per year is shown here. Grid lines are spaced every 5 degrees in latitude and longitude to aid identification of the AV location.

Atmospheric vortices typically have an organized oval shape, visually distinct from the surrounding atmosphere. This distinction is often identifiable in images. The images of the AV from Saturn's 2010 storm (Figure 2) clearly show such contrast at the vortex's boundary. Furthermore, a comparison between the wind/vorticity field (Sayanagi et al., 2013) and visual appearance indicates general consistency in identifying the AV's boundary. Therefore, we use visual inspection of the images to determine the AV boundary. Examples of AV boundaries determined by visual inspection are shown in the top two panels of Figure 2.

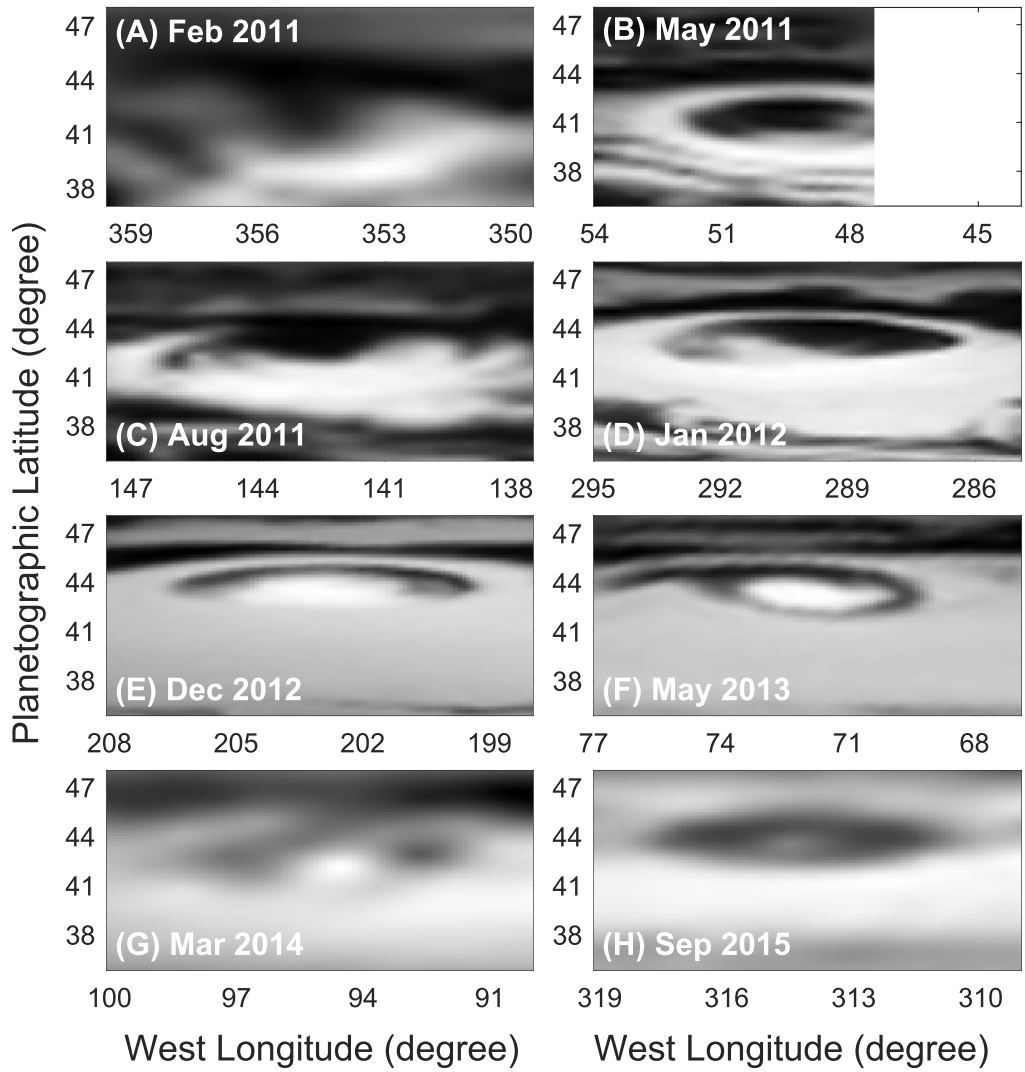

Figure 4. Time series of Cassini/VIMS maps at 5,000 nm illustrating the evolution of the anticyclonic vortex (AV) in deeper atmospheric layers (~2,000–5,000 mbar). The AV exhibits significant changes in morphology, size, and meridional position between February 2011 (panel a) and December 2012 (panel e), similar to the evolution observed in the CB2 images (Figure 2). The meridional range is identical across all panels to facilitate comparison of meridional drift and vortex size. Longitudes differ between panels due to the AV's longitudinal movement but span the same range (~10°) to allow comparison of longitudinal extent. Please note that the latitude and longitude ranges in these VIMS regional maps are smaller than those in the Cassini/Imaging Science Subsystem (ISS) (Figure 2) and HST/Wide Field Camera 3 (WFC3) (Figure 3) maps because the VIMS has far fewer pixels (32–64 across, compared with 256–1,024 for Cassini/ISS and 4,096 for HST/WFC3 UVIS) and therefore typically provides smaller spatial coverage when operating at relatively high spatial resolution. The maps were constructed from raw VIMS images with spatial resolutions ranging from ~240 to ~1,500 km/pixel (~0.26–1.61 degrees/pixel).

It should be noted that uncertainties exist in identifying the AV boundary regardless of the method used. For visual inspection, we assume an uncertainty of one pixel. Such an assumption is probably appropriate for the late stage of the AV (2012-) in which the AV has developed into a regular oval shape with a relatively clear boundary. But this assumption underestimates the uncertainty of the AV boundary in the early stage of the AV (2011). The other uncertainty source in determining the AV boundary comes from the navigation process, which typically introduces an error of approximately one pixel (e.g., L. Li et al., 2004). These two sources of uncertainty, visual inspection bias and navigation error, are combined to estimate the overall uncertainty in boundary determination. Since the determinations of AV size, location, and velocity are based on boundary measurements, the uncertainties in defining the boundary are propagated to those of size, location, and velocity following error propagation rules (Bevington & Robinson, 2003).

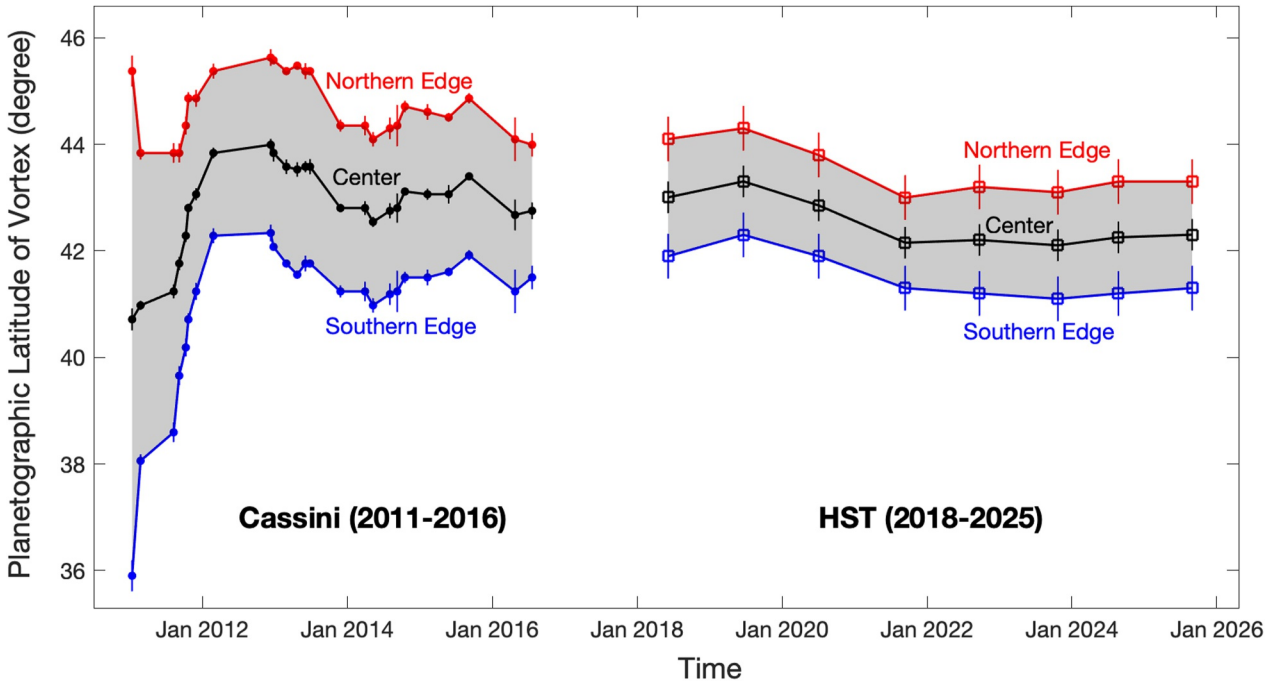

Figure 5. Time series of the anticyclonic vortex's latitudinal extent illustrating the temporal evolution of the vortex's meridional size and position. Major changes occur between 2011 and 2012, while after 2012, both the vortex center and its meridional extent remain largely stable with only minor variations. The measurements are derived from the Imaging Science Subsystem and HST maps (e.g., Figures 2 and 3). The vortex center is defined as the average latitude of its northern and southern edges. Vertical lines indicate measurement uncertainties.

Figure 5 presents the time series of the northern and southern edges as well as the center of the AV based on Cassini and HST observations. Assuming that the AV is centrally symmetric, which is valid for most of the time, the latitudinal position of the AV center is determined by averaging the latitudes of the southern and northern edges. The northern and southern edges of the AV are also used to determine its size in the meridional direction. Similarly, the eastern and western edges are used to define the center position and size of the AV in the longitudinal direction. The longitudinal and latitudinal positions of the AV center at different times are used to measure the zonal and meridional velocities of the AV as well.

Panel (a) of Figure 6 shows the time series of AV sizes in the zonal and meridional directions during both the Cassini and HST epochs. The zonal size decreased rapidly from ∼9,971 km in January 2011 to ∼4,844 km in October 2011 and then increased sharply to ∼6,758 km in February 2012. Afterward, it generally followed a decreasing trend through 2025. The pronounced changes in AV size between early 2011 and early 2012 are also evident in the regional maps (Figure S1 in Supporting Information S1), which show that the zonal extent of the vortex decreased substantially from January to October 2011 and then increased from October 2011 to January 2012. In the meridional direction, the temporal variations in AV size follow a pattern similar to that observed in the zonal direction.

We also investigated the aspect ratio of the AV, defined as the ratio of its zonal size to its meridional size, which plays an important role in AV stability (e.g., Aubert et al., 2012; Hassanzadeh et al., 2012; Ripa, 1987), with more circular vortices tending to be more stable (e.g., Carton & McWilliams, 1989; Flierl, 1988; Gent & McWilliams, 1986; Kloosterziel & Van Heijst, 1991; Polvani et al., 1989). Panel (b) of Figure 6 shows that the aspect ratio increased from late 2011 to early 2012, reaching a maximum of ∼2.2, corresponding to the rapid increase in zonal size (panel a). The subsequent decrease in the aspect ratio from early 2012 to mid-2013 is mainly due to the decrease in zonal size during this period. From 2013 to 2025, the aspect ratio oscillated but followed a long-term decreasing trend, reaching ∼1.1 in 2025.

Figure 7 presents the time series of the AV's zonal velocity, which suggests that the zonal velocity increased rapidly from ∼−11.0 m s^{-1} in January 2011 to ∼33.0 m s^{-1} in December 2012, then decreased to ∼6.5 m s^{-1} by July 2016. During the HST period, the zonal velocity decreased from ∼21.7 m s^{-1} in June 2018 to ∼4.1 m s^{-1} in

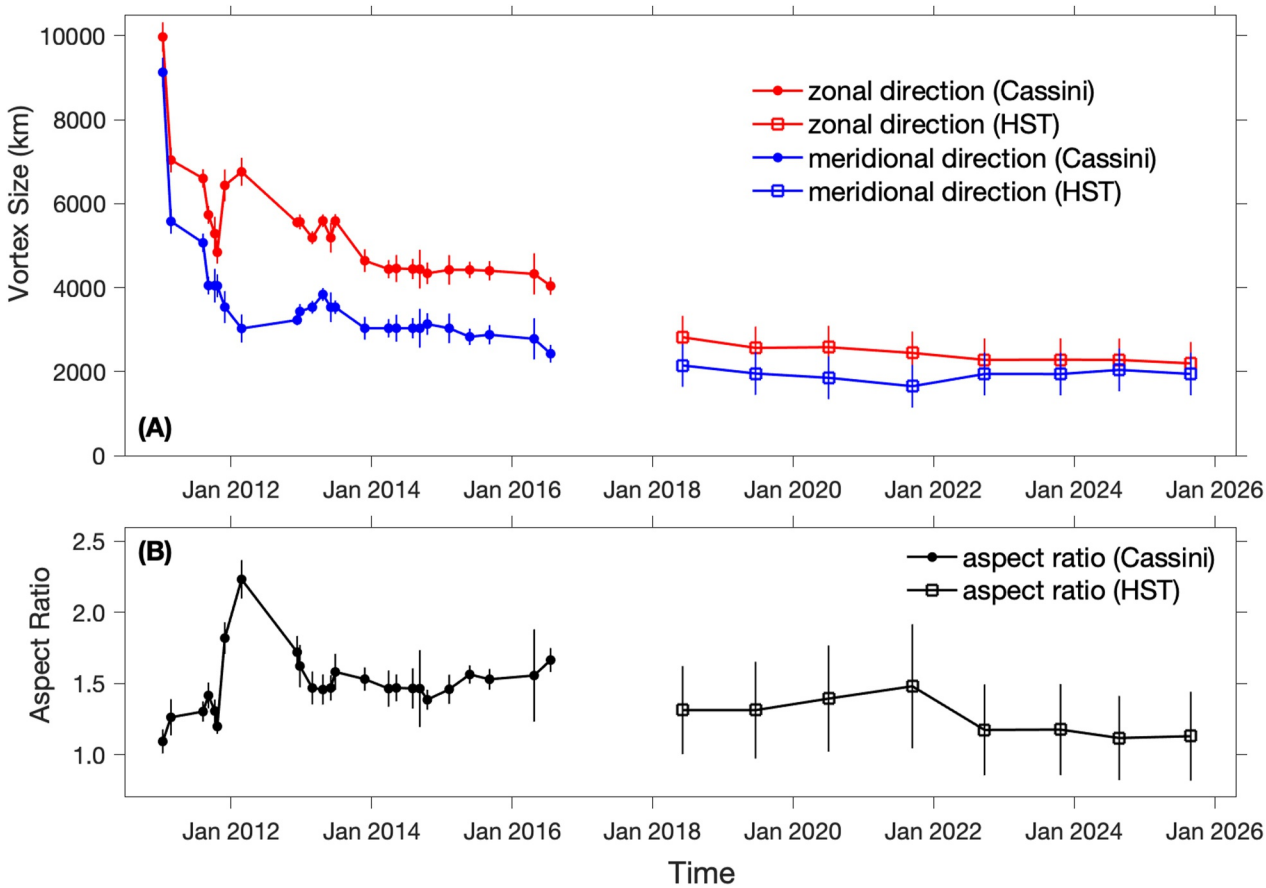

Figure 6. Time series of the anticyclonic vortex's (AV's) longitudinal and latitudinal sizes illustrating the temporal evolution of the vortex's horizontal dimensions and shape. Major changes occur during the early stages between 2011 and 2012, while afterward the sizes and shapes vary only weakly. (a) Longitudinal and latitudinal sizes representing the zonal and meridional extents of the vortex. (b) Aspect ratio (zonal size divided by meridional size) used to characterize the AV's shape. Vertical lines indicate measurement uncertainties. The measurements are derived from images recorded with the CB2 filter (~752 nm) by Cassini/Imaging Science Subsystem (2011–2016) and with the F763M filter (~761 nm) by HST/Wide Field Camera 3 (2018–2025).

October 2023, and then slightly increased to ~6.2 m s^{-1} in September 2025. These temporal variations are closely related to the background zonal winds, as shown in Figure 8. In particular, the rapid increase in velocity from January 2011 to December 2012 is mainly attributed to the northward drift of the AV during the same period (Figure 5).

Now let us discuss the AV's meridional drift (i.e., movement). Figure 5 shows that the most significant meridional movement of the AV, characterized by a northward drift, occurs in 2011 during the early stage of its evolution. After that, the AV exhibits relatively weak meridional motion: it oscillates in latitude during 2012–2021 and remains essentially stable near ~42.2° since 2021.

Meridional movement of vortices is generally related to the β-drift effect (e.g., Anthes & Hoke, 1975; Chan, 2005; Chan & Williams, 1987; Charney & Stern, 1962; Holland, 1984; X. Li & Wang, 1992; Rossby, 1948; Wang & Li, 1996). Here, we explore such an effect and its role in the meridional movement of the AV. The β-drift effect is generally controlled by the effective beta (β_e), which is defined as the meridional gradient of the zonal-mean quasi-geostrophic potential vorticity (also named as Qy). This parameter not only affects the meridional movement of vortices but also plays an important role in large-scale atmospheric dynamics (e.g., Andrews et al., 1987; Holton & Hakim, 2013; Pedlosky, 1987; Salby, 1996). The effective beta of Saturn's atmosphere has been estimated in previous investigations (e.g., L. Li et al., 2021; Read, Conrath, et al., 2009; Read, Dowling, et al., 2009; Wang et al., 2025).

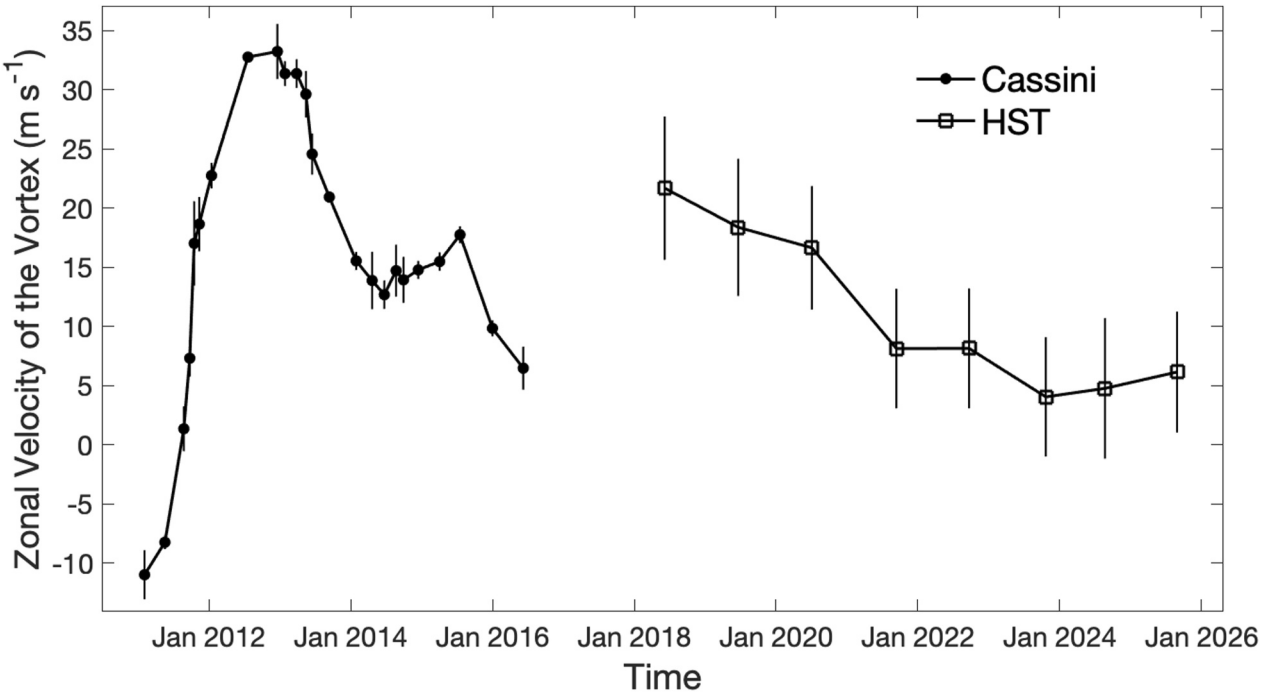

Figure 7. Time series of the anticyclonic vortex's (AV's) zonal velocity illustrating its temporal evolution. The most dramatic change occurs during the early stage between 2011 and 2012, when the zonal velocity increases from ∼−11 to ∼33 m/s. This increase is mainly attributed to the AV's northward migration caused by the β-drift effect, which moves the vortex from latitudes dominated by westward jets to those dominated by eastward jets. After 2012, the zonal velocity varies relatively weakly, which is also affected by the β-drift effect and background zonal jets. Vertical lines indicate measurement uncertainties. The long time intervals between the selected Cassini CB2 images (∼13–290 days) lead to relatively small uncertainties, whereas the ∼10-hr separation between the two HST maps each year results in larger uncertainties during the HST period.

The effective beta is expressed as $\beta_e = \beta + \beta_y + \beta_z$, where β is the planetary vorticity gradient, β_y is the gradient of zonal-mean relative vorticity, and β_z is the gradient of stretching vorticity. The third term (β_z) depends on the vertical shear of zonal winds, which is generally estimated indirectly from temperature fields via the thermal wind relation (e.g., L. Li et al., 2021; Read, Conrath, et al., 2009; Read, Dowling, et al., 2009; Wang et al., 2025). We did not find high-quality temperature fields at these latitudes, including the AV during the HST epoch. Additionally, the indirect estimates of β_z generally have large uncertainties (e.g., L. Li et al., 2021; Wang et al., 2025). Thus, we focus on the barotropic beta ($\beta_b = \beta + \beta_y$), which includes the planetary vorticity gradient (β) and the gradient of zonal-mean relative vorticity (β_y) only. The meridional gradient of the planetary vorticity can be expressed as $\beta = \partial f/\partial y = 2\Omega \cos \phi$, where f is Coriolis parameter ($f = 2\Omega \sin \phi$), Ω is the angular velocity of planet's rotation, and ϕ is latitude. When the zonal winds (u) is dominant over the meridional winds, the meridional gradient of the zonal-mean relative vorticity is defined as $\beta_y = -\partial^2 u/\partial y^2 = -u_{yy}$.

Because the most pronounced meridional movement occurred in 2011, we compute β_b using the 2011 zonal winds (Sayanagi et al., 2013). The β_b values in 2011 were already derived in our earlier work on the asymmetric expansion of bright clouds from the 2010 storm (L. Li et al., 2021), which is basically consistent with the results from other Cassini analyses (e.g., Del Genio et al., 2009; Read, Conrath, et al., 2009; Sánchez-Lavega et al., 2012). Here, we adopt them for analysis of the AV's meridional movement in the Cassini epoch. For the HST epoch (2018–2025), we use the zonal winds in 2020, which were measured by a previous study (Simon et al., 2021) to compute the barotropic beta.

Figure 9 shows the zonal winds and the corresponding β_b for the Cassini and HST epochs.

Panel (a) indicates that zonal wind uncertainties were much smaller for the Cassini epoch (2011) than for the HST epoch (2020) due to the superior spatial resolution of Cassini images. Consequently, β_b is much better constrained for Cassini than for HST (see panel b). Nonetheless, even the less precise HST estimates provide useful insight into the AV movement and stability. Panel (b) of Figure 9 shows that the Cassini β_b (red line) was negative from

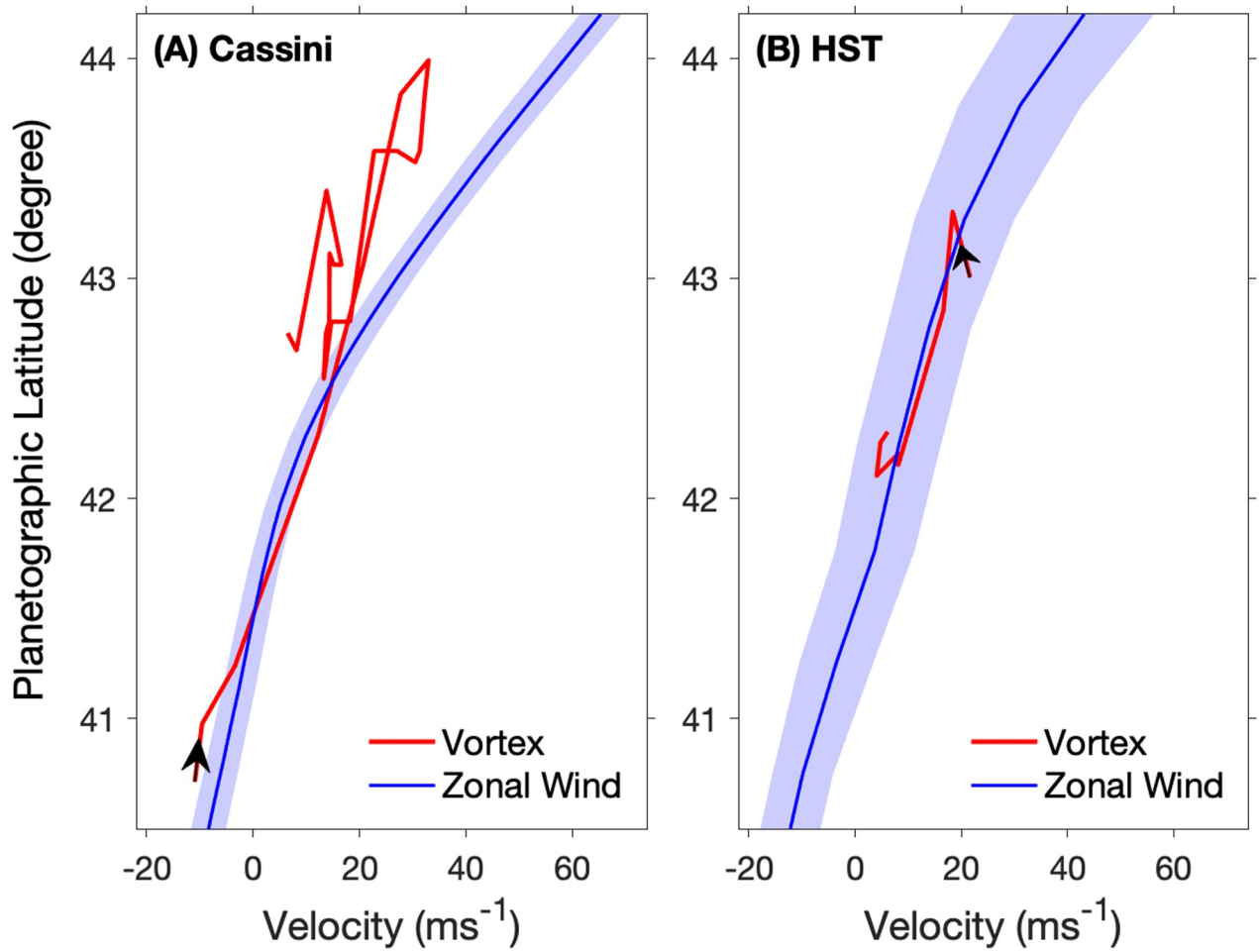

Figure 8. Comparison of the anticyclonic vortex's (AV's) zonal velocity with the background zonal winds. The AV's zonal velocity is basically consistent with the background zonal winds during the early Cassini stage and most of the HST observation period. (a) Cassini period (2011–2016). (b) HST period (2018–2025). Arrows indicate the starting points of the AV's zonal movement for each period. Blue shaded areas around the blue lines (background zonal winds) represent the uncertainties in the zonal-wind measurements.

the AV's initial latitude at 40.7° up to ∼43.0°. Because the AV is anticyclonic, this negative gradient implies that the AV would drift northward during the latitudinal range of 40.7°–43.0°, consistent with the observed meridional drift in 2011 (Figure 5). However, the AV did not stop at ∼43°, where $\beta_b = 0$. A possible explanation is an inertial overshoot from the northward motion during the latitudinal range of 40.7°–43.0°. Once the gradient turned positive above 43°, the β-drift effect forced a southward return toward the stable latitude at 43°, which was qualitatively consistent with the oscillations in the meridional movement from 2012 to 2016 as seen in Figure 5.

Panel (b) of Figure 9 also shows β_b for the HST epoch. It indicates a stable latitude ($\beta_b = 0$) near 42.6° for the AV (see blue line). The observed stable latitude for the AV at the late times of the HST epoch (2021–2025) is ∼42.2° (Figure 5), which is close to this theoretical value. The difference between theoretical prediction and observed value is probably related to the large uncertainties in estimating β_b in the HST epoch. It should be mentioned that other dynamical processes (e.g., eddies and storms) may also contribute to the meridional drift of the AV.

The β-drift theory not only predicts the drifting direction of vortices but also helps constrain the velocity of their meridional motion. Here, we first measure the meridional velocity of the AV and then compare the results with estimates from the β-drift theory. Measuring the meridional velocity is somewhat complex because it depends on the time scale considered. Based on the latitudinal center of the AV measured over long time intervals (∼13–290 days for Cassini and ∼1 year for HST), as shown in Figure 5, we derive long-term averaged meridional velocities (Figure 10). These results, obtained from measurements with a long time intervals, generally have relatively small uncertainties. Figure 10 shows that the rapid meridional motion of the AV during the early stage

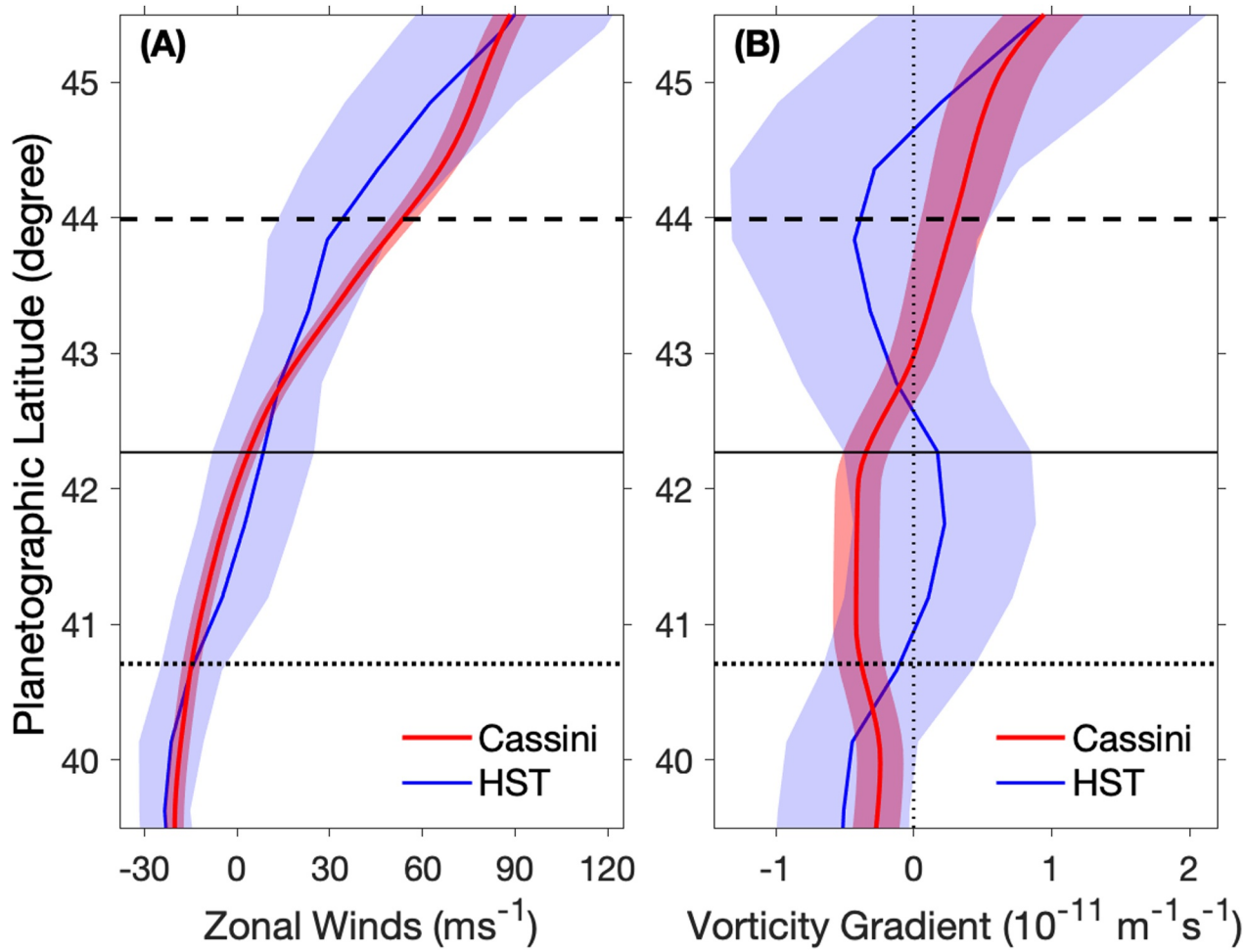

Figure 9. Zonal winds and barotropic stability (β_b) illustrating the dynamical environment controlling the anticyclonic vortex's (AV's) meridional drift. The negative β_b near the initial latitude of the AV during the early Cassini period (2011) indicates that the β-drift effect should push the vortex northward, consistent with the observed northward movement in the early stage. In contrast, β_b near the final latitude is close to zero, suggesting that the AV migrated into a dynamically stable latitude zone. (a) Zonal winds based on Cassini/Imaging Science Subsystem CB2 observations in 2011 and HST/Wide Field Camera 3 F631N observations in 2020. (b) β_b calculated from the zonal winds in panel (a). Shaded areas represent uncertainties. The solid horizontal line marks the final stable latitude of the AV (~42.2 degrees) estimated from the average vortex location during the HST period (2021–2025). The dotted and dashed horizontal lines indicate the initial latitude (~40.7 degrees in early 2011) and the northernmost latitude reached (~44.0 degrees in late 2012), respectively.

(2011) yields statistically significant meridional winds (i.e., velocities larger than the uncertainties) with a magnitude of ~0.46 m/s. However, such long-term averages may dilute stronger meridional velocities that occur on the shorter time scales. Our measurements based on two maps separated by approximately one rotation period (~10.6 hr) suggest that meridional velocities at the short time scale could be much stronger, reaching a magnitude of ~10 m/s. Unfortunately, the short time intervals also lead to large uncertainties, making these measurements at the short time scale statistically insignificant (i.e., uncertainties are comparable to the measured values).

Next, we discuss the theoretical prediction of the AV's meridional velocity based on the β-drift theory. The scaling law of β-drift (e.g., Charney & Stern, 1962; Holland, 1983; Marcus, 1993; McWilliams & Flierl, 1979; Rossby, 1948) can be used to estimate the velocity of meridional drifting for an isolated vortex, which is expressed as $V_\beta = -c\beta R^2$, where c is a constant depending on the vortex structure, β is represented by β_b in this investigation, and R is the vortex radius. Here we focus on the early stage of the AV (early to late 2011), during which it moved northward from ~40.7° to 43.0° with a maximum meridional velocity of ~0.46 m s^{-1} (see Figure 10). During this early stage, β_b was approximately $(-0.32 \pm 0.17) \times 10^{-11}$ m^{-1} s^{-1} (panel b of Figure 9) and R was ~5,800 km (panel a of Figure 6).

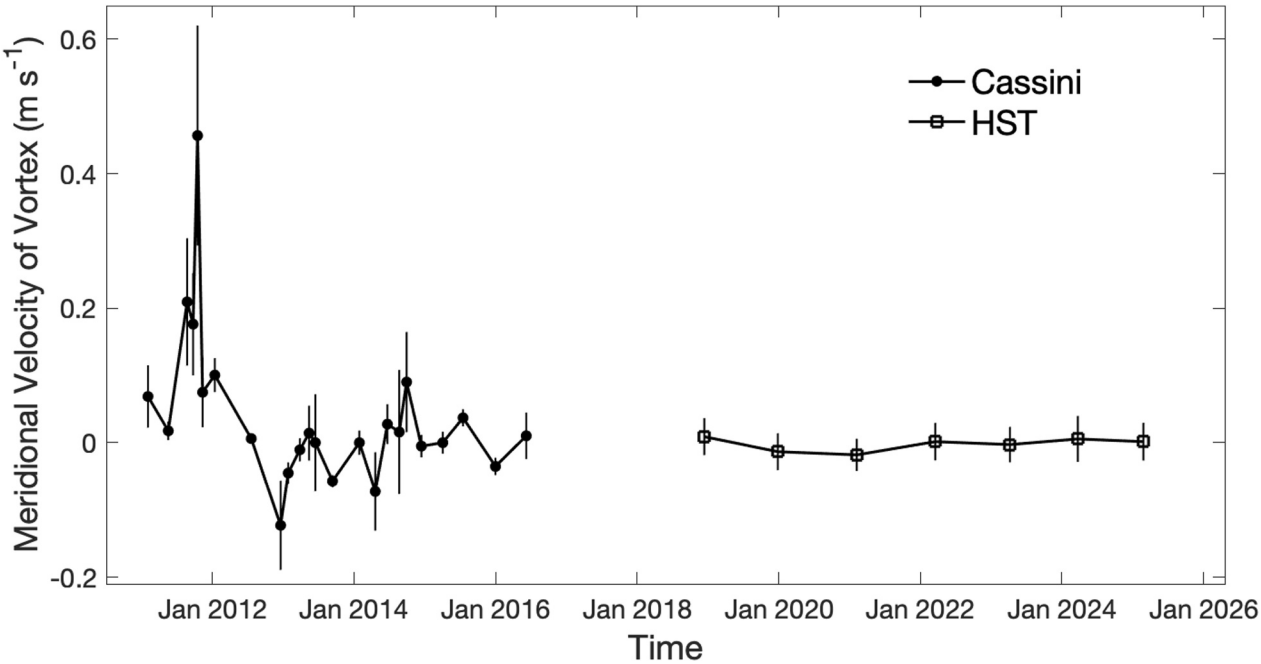

Figure 10. Time series of the anticyclonic vortex's (AV's) meridional velocity illustrating the temporal evolution of the AV's north-south movement. Significant meridional velocities occur during the early stage in 2011, whereas during most later times the meridional velocities are not statistically significant (i.e., smaller than the measurement uncertainties). The meridional velocity is derived from the latitudinal positions of the vortex center shown in Figure 5 using relatively long time intervals (13–290 days during the Cassini epoch and ∼1 year during the HST epoch). Vertical lines indicate measurement uncertainties. The uncertainties are generally smaller during the HST epoch than during the Cassini epoch because the time intervals used to derive the velocities are longer.

For typical isolated vortices in Earth's atmosphere, the constant c has values ranging from 0.2 to 0.5 (e.g., McWilliams & Flierl, 1979; Smith, 1993; Smith et al., 1997). Using the medium value (c = 0.35), the theoretical β-drift velocity ($V_\beta = -c\beta R^2$) is estimated as 18–58 m s^{-1} for the AV case. This estimate is significantly larger than the observed average meridional velocity of the AV over longer time scales (∼0.46 m s^{-1}), although the short time scale meridional velocities may approach the lower bound of the theoretical predictions.

3.2. Vertical Structure and Spectral Characteristics of the AV

After examining the AV's temporal evolution and dynamics based primarily on observations probing the top visible clouds (NH_3), we investigate its vertical structure. Both Cassini and HST observations cover different wavelengths, allowing them to probe different atmospheric layers. Here we examine the vertical structure of the vertex, first using Cassini ISS and VIMS observations, and then HST/WFC3 images.

Based on the scattering and absorption properties of Saturn's gases and aerosols (e.g., Sromovsky et al., 2016, 2021; West et al., 2009) as well proposed cloud compositions (e.g., Atreya & Wong, 2005; Atreya et al., 1999; Simon et al., 2022), radiative transfer analyses have estimated the vertical distribution of hazes and cloud decks in Saturn's upper atmosphere (e.g., Fletcher, Baines, et al., 2011; Fletcher, Hesman, et al., 2011; Oliva et al., 2016; Pérez-Hoyos et al., 2005, 2016; Porco et al., 2004; Roman et al., 2013; Sanz-Requena et al., 2019; Sromovsky et al., 2013, 2016, 2021). Although some discrepancies exist among studies, a broadly consistent structure has emerged: stratospheric hazes at ∼10–100 mbar; tropospheric hazes at ∼100–500 mbar; ammonia (NH_3) clouds at ∼500–1,500 mbar; ammonium hydrosulfide (NH_4SH) clouds at ∼2,000–5,000 mbar; and water (H_2O) clouds at ∼5,000–15,000 mbar.

The stratospheric hazes around 10–100 mbar are primarily sensed by images recorded at ultraviolet wavelengths and strong methane absorption bands (e.g., ∼890 nm). The pressure levels including NH_3 clouds (500–1,500 mbar) can be probed by images recorded at continuum bands, such as the one around 750 nm. The

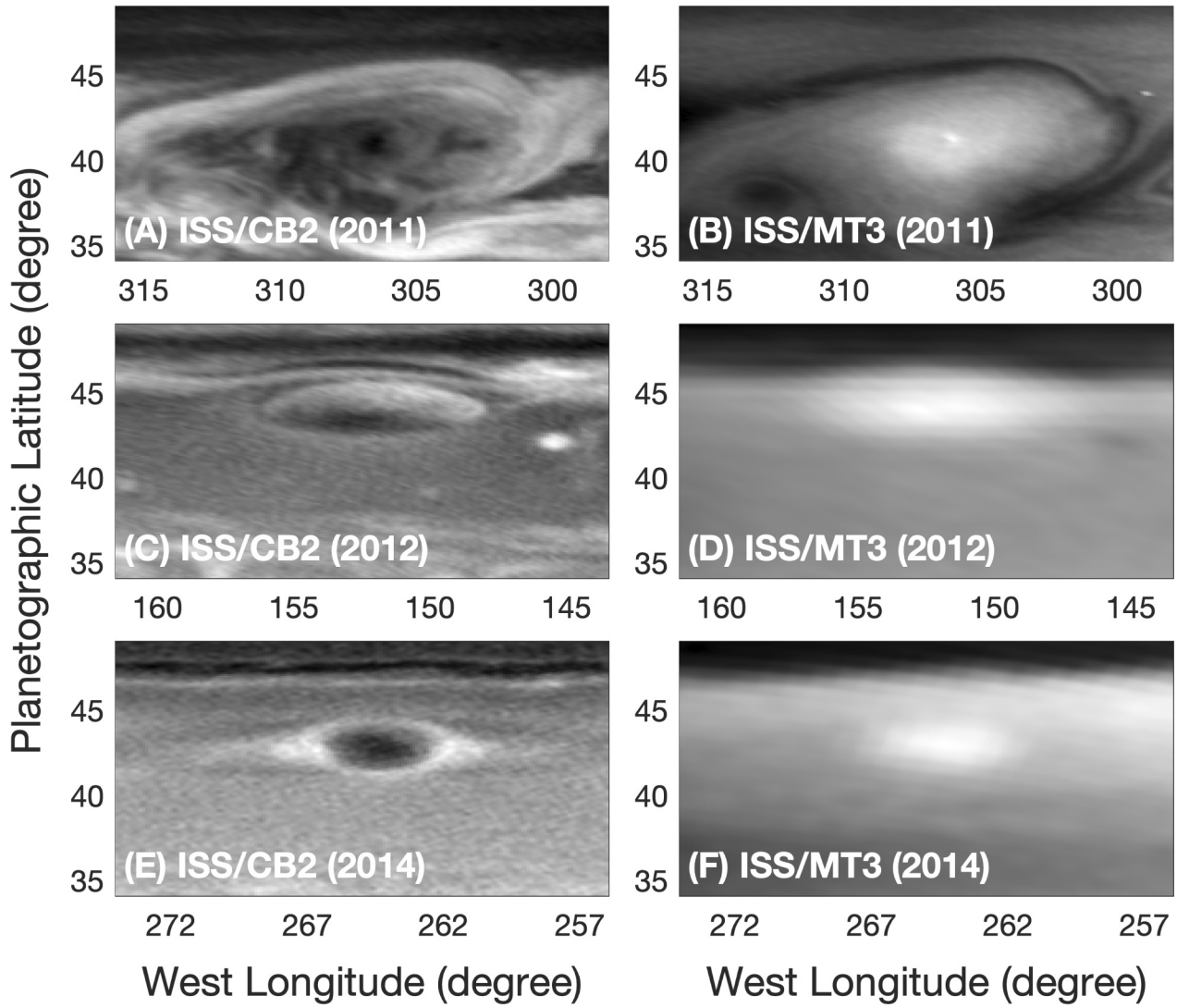

Figure 11. Comparison of the anticyclonic vortex (AV) in Cassini/Imaging Science Subsystem CB2 and MT3 images illustrating its wavelength-dependent appearance and vertical structure. The AV appears brighter than its surroundings in the MT3 images, suggesting that the upper portion of the vortex contains stratospheric haze particles that strongly scatter sunlight at the MT3 wavelength. Latitudes and longitudinal ranges are kept the same in each year to facilitate comparison between CB2 and MT3. The CB2 and corresponding MT3 images in each year are separated by ∼17–23 s, making them quasi-simultaneous observations. The raw CB2 images used to generate the maps in panels (a), (c), and (e) have spatial resolutions of 123 km/pixel (∼0.13 degrees/pixel), 118 km/pixel (∼0.13 degree/pixel), and 171 km/pixel (∼0.18 degrees/pixel), respectively. The raw MT3 images used to generate the maps in panels (b), (d), and (f) have spatial resolutions of 123 km/pixel (∼0.13 degrees/pixel), 473 km/pixel (∼0.51 degrees/pixel), and 682 km/pixel (∼0.73 degrees/pixel), respectively. The lower spatial resolutions of the MT3 images in panels (d) and (f) result from the use of different pixel modes during recording (256 × 256 for MT3 and 1,024 × 1,024 for CB2).

pressure levels including NH_4SH clouds (5,000–15,000 mbar) are generally investigated using 5000-nm observations.

Figure 11 compares the AV in the Cassini/ISS images between CB2 (∼752 nm) and MT3 (∼889 nm) filters. The presence of the AV in both indicates that it spans from the ammonia-cloud levels (∼500–1,500 mbar) to the pressure levels of stratospheric hazes (∼10–100 mbar). In the images recorded at the MT3 filter, the AV appears brighter than its surroundings, consistent with enhanced scattering from stratospheric haze particles at this wavelength (e.g., Sromovsky et al., 2016, 2021; West et al., 2009).

The VIMS observations provide more information on the vertical structure of the AV. Although simultaneous observations between Cassini/ISS and Cassini/VIMS are rare, we identified quasi-simultaneous observations by searching the entire Cassini data archive. These quasi-simultaneous observations provide an opportunity to cross-

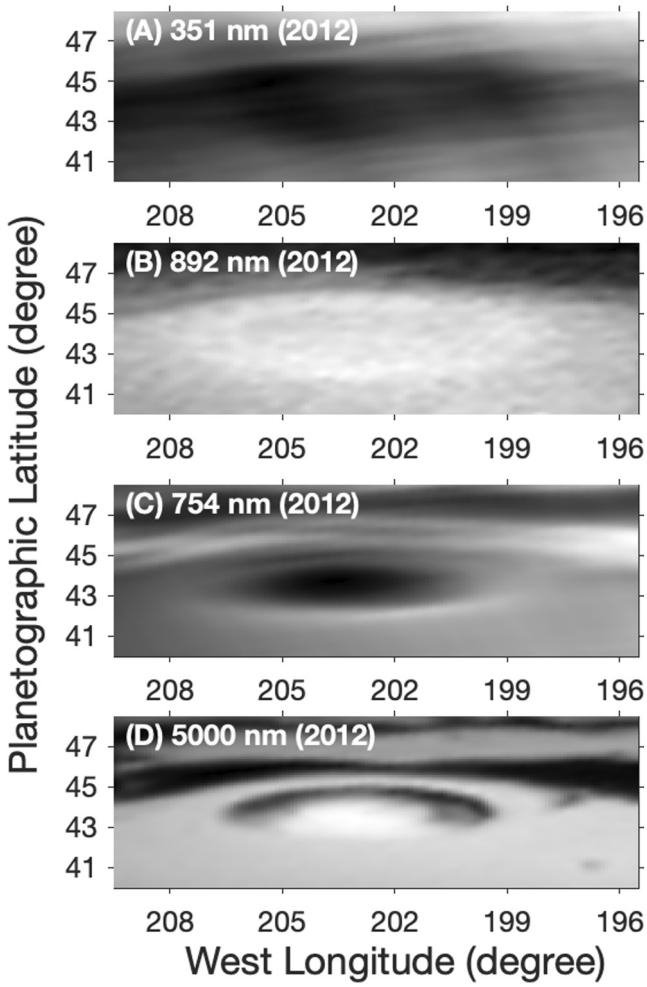

Figure 12. Cassini/VIMS multi-wavelength maps illustrating the anticyclonic vortex's (AV's) large vertical extent. The appearance of the AV in the 351-nm images suggests that the top of the AV reaches the stratospheric haze layers at ∼10–100 mbar, while the detection of the AV in the 5000-nm image indicates that the base of the vortex extends at least to pressure levels near the NH_4SH cloud layer (∼2,000–5,000 mbar). (a) The ultraviolet image at 351 nm primarily probes the stratospheric haze layers at pressures of ∼10–100 mbar. (b) The image recorded by the strong methane absorption band at 892 nm samples similar stratospheric haze layers. (c) The continuum-band image at 754 nm mainly detects the top NH_3 cloud deck at ∼500–1,500 mbar. (d) The image at 5,000 nm probes deeper atmospheric layers, including the NH_4SH clouds around ∼2,000–5,000 mbar. The spatial resolutions of the raw images used to generate the multi-wavelength maps are ∼320 km/pixel (∼0.34 degrees/pixel).

validate both the ISS and VIMS data sets. Figure S2 in Supporting Information S1 compares ISS and VIMS images separated by ∼1.4 days. The VIMS recorded images at many more wavelengths than the ISS, so for comparison we selected the VIMS images at wavelengths closest to the ISS CB2 and MT3 filters. The comparison shows that the AV essentially exhibits the same appearance in both the ISS and VIMS observations. The relatively small discrepancies between the two data sets can be attributed to slight differences in wavelength, viewing geometry, and observation time.

After validating the VIMS observations, we use them to further constrain the vertical structure of AV. Figure 12 displays the VIMS images at four representative wavelengths: 351 nm, the shortest wavelength in the VIMS range representing the ultraviolet; 892 nm, corresponding to the ISS/MT3 filter for the strongest methane absorption band; 754 nm, a continuum band corresponding to the ISS/CB2 filter; and 5,000 nm, probing deeper atmospheric layers. As discussed above, images recorded at ultraviolet wavelengths and the strong methane absorption band mainly probe pressure levels including stratospheric hazes (10–100 mbar), whereas images recorded in the continuum bands sense deeper levels with tropospheric clouds. In particular, the 754-nm images sense atmospheric layers containing NH_3 clouds (∼500–1,500 mbar), while the 5000-nm images probe even deeper layers with NH_4SH clouds (∼2,000–5,000 mbar).

The AV is clearly visible at all four wavelengths, indicating a substantial vertical extent from the stratospheric hazes (∼10–100 mbar) down to the deep NH_4SH cloud layer (∼2,000–5,000 mbar). Assuming a constant scale height of ∼59.5 km (Archinal et al., 2018) from the lower stratosphere to the upper troposphere, and taking the stratospheric hazes to be centered at ∼55 mbar (the midpoint of the 10–100 mbar range) and the deep NH_4SH cloud layer to be centered at ∼3,500 mbar (the midpoint of the 2,000–5,000 mbar range), the AV's vertical extent is estimated to be at least ∼250 km.

The HST/WFC3 multi-filter images can help us better understand the vertical structure of the vortex. Figure 13 shows HST/WFC3 images at multiple wavelengths. The FQ889N filter (panel c, 889 nm), analogous to Cassini/MT3, also reveals a bright vortex. In contrast, ultraviolet images at F343N (panel b, 344 nm) show the AV as dark. Both filters (FQ889N and F343N) probe the pressure levels of the stratospheric haze. However, the haze aerosols strongly scatter solar radiance at 889 nm (FQ889N) but absorb it at 344 nm (F343N) in the ultraviolet (Sromovsky et al., 2016, 2021; West et al., 2009). This explains the opposite vortex contrast between the two filters. At an even shorter wavelength (236 nm; panel a), the HST images probe higher altitudes than those recorded at 344 nm because Rayleigh scattering is stronger at shorter wavelengths. The AV is still visible in the 236 nm images, suggesting that it has a substantial vertical extent in the lower stratosphere.

The HST/WFC3 multi-wavelength images are also used to derive the Color Index (CI) and Altitude-Opacity Index (AOI) to characterize the cloud and haze properties of the AV, following the methodology of previous studies (de Pater et al., 2010; Sánchez-Lavega et al., 2013; Wong et al., 2011). We first define the relative reflectivity at different wavelengths, $R(\lambda)$, as the reflectivity ratio between the feature of interest and a reference region that is relatively uniform and lacks identifiable structures (Sánchez-Lavega et al., 2013).

In this study, $R(\lambda)$ is defined as the ratio of reflectivity between the AV center and a reference point at the same latitude outside the AV, and the CI is defined as the ratio of $R(\lambda)$ between the HST blue and red wavelengths, represented by F467M (∼468 nm) and F631N (∼630 nm), respectively. Red features, such as Jupiter's GRS and Red Oval (RO), typically have CI $<$ 1, while white features generally exhibit CI $\geq$ 1 (Sánchez-Lavega

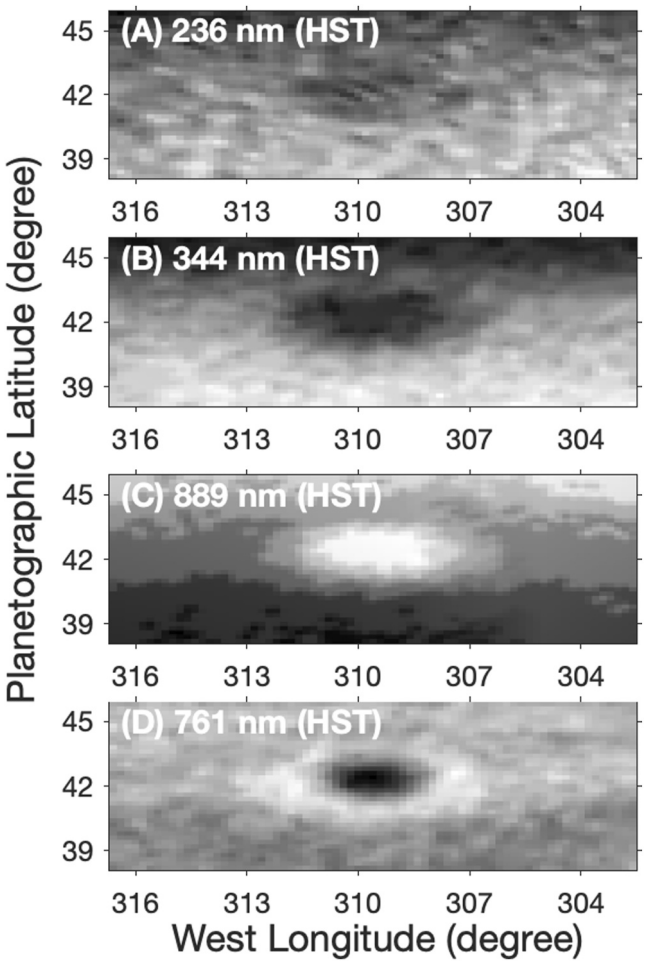

Figure 13. HST/Wide Field Camera 3 (WFC3) multi-wavelength maps illustrating the anticyclonic vortex's (AV's) vertical extent. The appearance of the AV in images at different wavelengths, which probe different atmospheric altitudes, reveals the substantial vertical extent of the vortex. The raw WFC3 images used to create the maps in panels (a–d) were recorded with filters F225W, F343N, FQ889N, and F763M, respectively, which have central wavelengths of 236, 344, 889, and 761 nm. These images were taken with time intervals of 4–7 min and have similar spatial resolutions of ~300 km/pixel (~0.32 degrees/pixel). Therefore, these maps can be considered quasi-simultaneous.

et al., 2013). The AOI is defined as the ratio of $R(\lambda)$ between the HST methane absorption and ultraviolet bands, represented by FQ889N (~889 nm) and F275W (~270 nm), respectively. The AOI provides insight into haze layer characteristics. Typical AOI values are around 1, with smaller values indicating relatively low and thin haze layers, and larger values implying higher and denser haze layers (Sánchez-Lavega et al., 2013).

Using the above definitions of CI and AOI with the selected reference points (see Figure 14), we compute the two indices for the AV, yielding values of 1.0 and 1.4 for CI and AOI, respectively. Jupiter's long-lived GRS and RO exhibit AOI values of about 1.4 (Sánchez-Lavega et al., 2013), suggesting that Saturn's long-lived AV has a haze structure similar to that of Jupiter's GRS and RO, with all of these vortices characterized by relatively high and dense haze layers (Baines et al., 2009; Sánchez-Lavega et al., 2013). For the CI, Jupiter's GRS and RO have values less than 1 (0.56 and 0.8 for the GRS and RO, respectively), whereas the tropical white ovals display relatively large values of around 1.0. The CI value of the AV (1.0) therefore indicates that it is analogous to Jupiter's tropical white ovals (CI = 1.04), which are spectrally flat features (Sánchez-Lavega et al., 2013).

4. Discussion

As shown in Figures 2–6, the AV changed its size and shape during its temporal evolution. It developed a compact and quasi-circular shape with an aspect ratio close to unity (Figure 6). This suggests that the AV tended to become more stable over time, because more circular vortices are generally more stable (e.g., Carton & McWilliams, 1989; Flierl, 1988; Gent & McWilliams, 1986; Kloosterziel & Van Heijst, 1991; Polvani et al., 1989). For comparison, the average aspect ratio of Saturn's anticyclones is ~2.0 (Trammell et al., 2014, 2016; Vasavada et al., 2006). Thus, the small aspect ratio at the end of our observation period (~1.1) suggests that this AV is more stable than typical Saturnian anticyclones.

Analysis of the zonal velocity of the AV (Figures 7 and 8) suggests that the background zonal winds play a critical role in the longitudinal motion of the AV. However, the zonal velocity of the AV is significantly smaller than that of the background zonal winds during the late part of the Cassini epoch. We do not have a definitive explanation for this discrepancy, although interactions between the AV and the surrounding turbulent environment may play a role. During the HST epoch, the temporal decrease in the AV's zonal velocity is generally consistent with the background zonal winds, which results from the southward drift of the AV. In summary, the combination of the AV's meridional drift and the background zonal winds plays a critical role in determining the AV's zonal velocity. This raises an important question: why did the AV drift meridionally?

The β-drift effect generally plays an important role in the meridional motion of vortices (e.g., Anthes & Hoke, 1975; Chan, 2005; Chan & Williams, 1987; Charney & Stern, 1962; Holland, 1984; X. Li & Wang, 1992; Rossby, 1948; Wang & Li, 1996). Examination of the barotropic vorticity gradient (Figure 9) suggests that the meridional drift of the AV is indeed affected by the β-drift effect. A quantitative comparison between theoretical estimates and measured meridional velocities (Figure 10) reveals a discrepancy. This discrepancy may be due to several factors: (a) the time scale of the wind measurements may play a role; (b) Saturn may have a different effective value of the constant c compared with Earth; (c) the uncertainty in determining barotropic vorticity gradient may be underestimated; and (d) interactions between the AV and its surrounding environment (e.g., clouds and eddies) may play a significant role in its meridional motion, such that the AV cannot be treated as an isolated system.

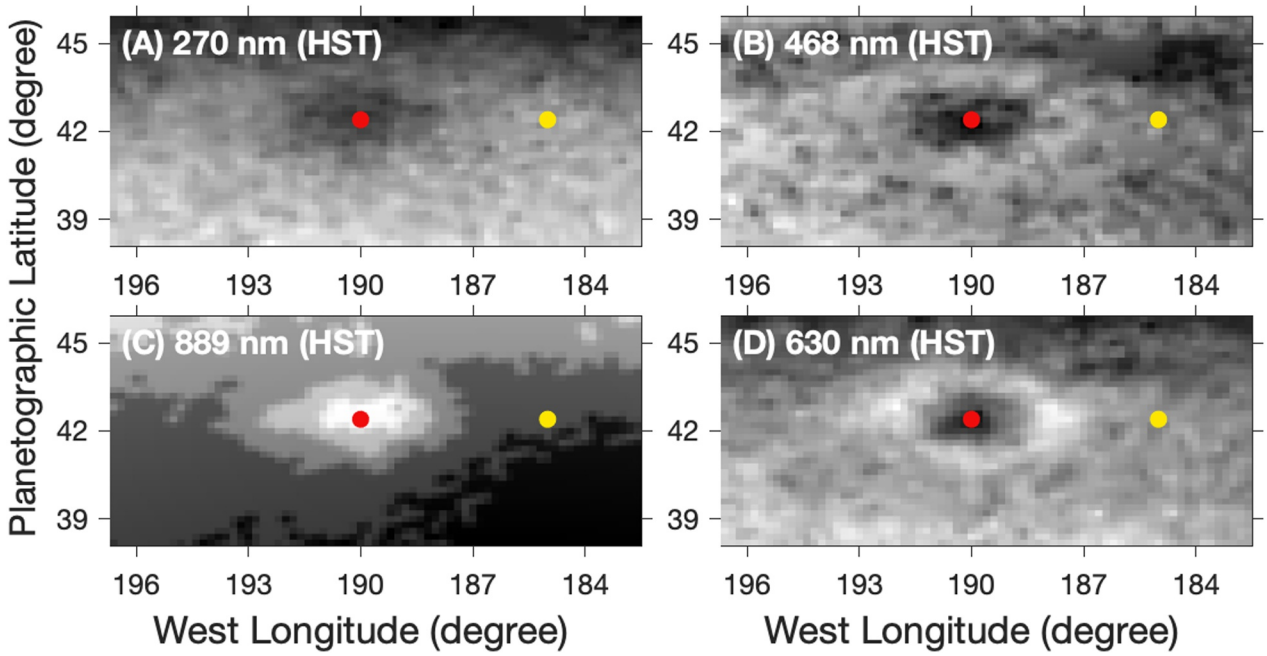

Figure 14. HST/Wide Field Camera 3 maps at four wavelengths were used to derive the Color Index and Altitude-Opacity Index. (a) F275W with a central wavelength ~270 nm. (b) F467M with a central wavelength ~468 nm. (c) FQ889N with a central wavelength ~889 nm. (d) F631N with a central wavelength ~630 nm. The four images displayed in the four panels have similar spatial resolutions of ~300 km/pixel (~0.32 degrees/pixel). The red dot in each panel marks the anticyclonic vortex (AV) center, and the yellow dot indicates the reference area outside the AV. Please refer to the main text for a discussion of the selection of the four filters and their corresponding wavelengths.

In the vertical direction, the presence of the AV at different wavelengths (Figures 11–13), which are sensitive to different pressure levels, suggests that the AV has a substantial vertical extent of more than 250 km. Analysis of the VIMS images and spectra (Figures S3-S4 in Supporting Information S1) provides insight into the temporal evolution of the AV's vertical structure. Figure S3 in Supporting Information S1 shows that the northwest portion of the AV appears bright at 754 nm (panel a) but dark at 5,000 nm (panel e) in the early stage (2011), indicating the presence of upper-tropospheric clouds (NH_3, NH_4SH, or both) that reflect sunlight at 754 nm and block thermal emission from the deep atmosphere sensed by the 5000-nm images. In contrast, the southeast portion is dark at 754 nm and bright at 5,000 nm, suggesting a relatively cloud-free region.

Figure S3 in Supporting Information S1 also suggests that the cloud distribution evolves from August 2011 (panels a and e) to January 2012 (panels b and f), with clouds shifting from the northwest toward the northeast, possibly as a result of the rotation of the anticyclone. Between January 2012 (panels b and f) and December 2012 (panels c and g), the upper-tropospheric cloud structure became more symmetric. By December 2012, the vortex center appeared dark at 754 nm but bright at 5,000 nm, while the periphery showed the opposite behavior. This center–periphery contrast remains stable through 2015 (panels d and h), although the relative areas evolve: the dark central region shrinks while the bright outer region expands at 754 nm (panels c and d), and correspondingly the bright center shrinks while the dark periphery expands at 5,000 nm (panels g and h). These trends indicate an increasing spatial extent of upper-tropospheric clouds within the vortex.

To examine the spectral properties associated with the temporal variations, we select pairs of grid points with opposite brightness within the AV in the VIMS images and compare their spectra (Figure S4 in Supporting Information S1). The red lines represent spectra for regions that are bright in the 754 nm images but dark in the 5,000 nm images (see points A, C, E, and G in Figure S3 in Supporting Information S1). In contrast, the blue lines represent spectra for regions with the opposite appearance: dark in the 754 nm images but bright in the 5,000 nm images (see points B, D, F, and H in Figure S3 in Supporting Information S1). Here, we focus on the spectral behavior near 5,000 nm. Figure S4 in Supporting Information S1 shows that the bright regions in the 5000-nm images (points B, D, F, and H in Figure S3 in Supporting Information S1), which are associated with cloud-free areas, exhibit enhanced radiance (represented by the reflectivity in Figure S4 in Supporting Information

S1) near 5,000 nm compared with the darker regions (points A, C, E, and G). More importantly, the spectral analysis reveals a notable temporal trend in this enhanced radiance: the spectral range of enhanced radiance narrows significantly from ∼4,500 to 5,000 nm in December 2012 (panel c of Figure S4 in Supporting Information S1) to ∼4,900–5,000 nm in September 2015 (panel d of Figure S4 in Supporting Information S1). Such a narrowing likely suggests a reduction in cloud-free areas, implying an increase in the horizontal coverage, the vertical extent, or both, of the upper clouds within the AV, although variations in cloud properties may also contribute to the changes in the spectral shape (Sromovsky et al., 2013). This interpretation is consistent with the increasing spatial extent of upper-tropospheric clouds inferred from the images shown in Figure S3 in Supporting Information S1. Taken together, the VIMS spectral and imaging analyses indicate strengthening cloud formation as the AV evolves.

5. Conclusions

Based on long-term multi-wavelength observations from Cassini and HST, we investigate the temporal evolution, meridional drift, vertical structure, and spectral characteristics of the AV generated by Saturn's 2010 giant convective storm.

Our analysis shows that the AV has persisted for more than 14 years (2011–2025). The AV undergoes its most significant changes in size, morphology, aspect ratio, and velocity during the early stage (2011–2012), followed by relatively weak variations. In particular, the AV has become basically stable in the late HST epoch (2022–2025). Over time, the vortex evolved into a more compact and organized structure with a nearly axisymmetric morphology. Its appearance at multiple wavelengths probing different atmospheric layers indicates a vertical extent exceeding ∼250 km (∼4.2 scale heights) spanning from the upper troposphere to the lower stratosphere. Analysis of barotropic vorticity gradients suggests that the AV eventually migrated to latitudes where meridional drift is weak, suggesting that the vortex has entered a relatively stable stage and may persist for an extended period.

These observations provide the most complete timeline to date of the formation and long-term evolution of a large anticyclonic vortex produced by a major convective storm in a giant planet atmosphere. The origin and persistence of the AV likely reflect the unique dynamic environment of Saturn's atmosphere. Saturnian vortices evolve within a deep atmosphere lacking a lower solid boundary. In such environments, internal heat, atmospheric stratification, and vertical coupling between atmospheric layers likely play central roles in controlling vortex dynamics and long-term stability. Further theoretical and numerical studies are needed to investigate how these processes influence the evolution of large vortices generated by moist convection.

Comparisons with vortices observed on other planets provide additional context for interpreting these results. Long-lived anticyclones are also present in Jupiter's atmosphere (e.g., Bolton et al., 2021), although differences in background circulation, thermal structure, and internal heat between Jupiter and Saturn likely contribute to the distinct vortex populations observed on the two planets (e.g., Trammell et al., 2014). Recent observations of vortices on Neptune (Wong et al., 2018, 2019, 2022) further demonstrate that large anticyclonic vortices are a common feature of giant-planet atmospheres, although the mechanisms controlling their formation and longevity remain uncertain. Together, these comparisons highlight the importance of cross-planet studies for identifying both universal and planet-specific aspects of vortex dynamics.

In summary, the observational characteristics of Saturn's long-lived vortex provide important constraints on the dynamics of giant-planet atmospheres and offer a valuable reference case for future theoretical and numerical investigations of vortex evolution in planetary atmospheres.

Conflict of Interest

The authors declare no conflicts of interest relevant to this study.

Availability Statement

The Cassini data used in this study are publicly available through NASA's Planetary Data System: Imaging Science Subsystem (ISS) (Porco & Cassini Imaging Science Team, 2020) and Visual and Infrared Mapping Spectrometer (VIMS) (Brown & VIMS Science Team, 2020). The HST data are publicly available through the MAST archive at

the Space Telescope Science Institute: Outer Planet Atmospheres Legacy (OPAL) (Simon, 2015). The processed data of the vortex's characteristics are available on Zenodo (Wang, 2026).

Acknowledgments
We are grateful to the Cassini ISS and VIMS teams for recording the raw data sets and to the HST OPAL program for providing the global maps of Saturn. Liming Li acknowledges the support received from the NASA ROSES Cassini Data Analysis Program and NSF Astronomy and Astrophysics Research Grants.

References

Adriani, A., Mura, A., Orton, G., Hansen, C., Altieri, F., Moriconi, M. L., et al. (2018). Clusters of cyclones encircling Jupiter's poles. *Nature*, *555*(7695), 216–219. https://doi.org/10.1038/nature25491

Andrews, D. G., Holton, J. R., & Leovy, C. B. (1987). *Middle atmosphere dynamics*. Academic Press.

Anthes, R. A., & Hoke, J. E. (1975). The effect of horizontal divergence and the latitudinal variation of the Coriolis parameter on the drift of a model hurricane. *Monthly Weather Review*, *103*(9), 757–763. https://doi.org/10.1175/1520-0493

Archinal, B. A., Acton, C. H., A'Hearn, M. F., Conrad, A., Consolmagno, G. J., Duxbury, T., et al. (2018). Report of the IAU working group on cartographic coordinates and rotational elements: 2015. *Celestial Mechanics and Dynamical Astronomy*, *130*(3), 1–46. https://doi.org/10.1007/s10569-017-9805-5

Atreya, S. K., & Wong, A. S. (2005). Coupled clouds and chemistry of the giant planets—A case for multiprobes. *Space Science Reviews*, *116*(1–2), 121–136. https://doi.org/10.1007/s11214-005-1951-5

Atreya, S. K., Wong, M. H., Owen, T. C., Mahaffy, P. R., Niemann, H. B., de Pater, I., et al. (1999). A comparison of the atmospheres of Jupiter and Saturn: Deep atmospheric composition, cloud structure, vertical mixing, and origin. *Planetary and Space Science*, *47*(10–11), 1243–1262. https://doi.org/10.1016/S0032-0633(99)00047-1

Aubert, O., Le Bars, M., Le Gal, P., & Marcus, P. S. (2012). The universal aspect ratio of vortices in rotating stratified flows: Experiments and observations. *Journal of Fluid Mechanics*, *706*, 34–45. https://doi.org/10.1017/jfm.2012.188

Baines, K. H., Delitsky, M. L., Momary, T. W., Brown, R. H., Buratti, B. J., Clark, R. N., & Nicholson, P. D. (2009). Storm clouds on Saturn: Lightning-induced chemistry and associated materials consistent with Cassini/VIMS spectra. *Planetary and Space Science*, *57*(14–15), 1650–1658. https://doi.org/10.1016/j.pss.2009.06.025

Baines, K. H., Drossart, P., Momary, T. W., Formisano, V., Griffith, C. A., Bellucci, G., et al. (2005). The atmospheres of Saturn and Titan in the near-infrared: First results of Cassini/VIMS. *Earth, Moon, and Planets*, *96*(3–4), 119–147. https://doi.org/10.1007/s11038-005-9058-2

Baines, K. H., Sromovsky, L. A., Carlson, R. W., Momary, T. W., & Fry, P. M. (2019). The visual spectrum of Jupiter's great Red Spot accurately modeled with aerosols produced by photolyzed ammonia reacting with acetylene. *Icarus*, *330*, 217–229. https://doi.org/10.1016/j.icarus.2019.04.008

Baines, K. H., Sromovsky, L. A., Fry, P. M., Momary, T. W., Brown, R. H., Buratti, B. J., et al. (2018). The eye of Saturn's north polar vortex: Unexpected cloud structures observed at high spatial resolution by Cassini/VIMS. *Geophysical Research Letters*, *45*(12), 5867–5875. https://doi.org/10.1029/2018GL078168

Barnes, J. W., Brown, R. H., Soderblom, L., Buratti, B. J., Sotin, C., Rodriguez, S., et al. (2007). Global-scale surface spectral variations on Titan seen from Cassini/VIMS. *Icarus*, *186*(1), 242–258. https://doi.org/10.1016/j.icarus.2006.08.021

Bevington, P. R., & Robinson, D. K. (2003). *Data reduction and error analysis for the physical sciences* (3rd ed.). McGraw-Hill.

Bolton, S. J., Levin, S. M., Guillot, T., Li, C., Kaspi, Y., Orton, G., et al. (2021). Microwave observations reveal the deep extent and structure of Jupiter's atmospheric vortices. *Science*, *374*(6570), 968–972. https://doi.org/10.1126/science.abf1015

Brown, R. H., Baines, K. H., Bellucci, G., Bibring, J. P., Buratti, B. J., Capaccioni, F., et al. (2004). The Cassini visual and infrared mapping spectrometer (VIMS) investigation [Dataset]. *Space Science Reviews*, *115*(1–4), 111–168. https://doi.org/10.1007/s11214-004-1453-x

Brown, R. H., & VIMS Science Team. (2020). VIMS observations from the Cassini tour of the Saturn system. In *NASA planetary data System, urn:nasa:pds:cassini_vims_saturn::1.0*. https://doi.org/10.17189/1504134

Carton, X. J., & McWilliams, J. C. (1989). Barotropic and baroclinic instabilities of axisymmetric vortices in a quasigeostrophic model. In B. J. Rothschild (Ed.), *Mesoscale/synoptic coherent structures in geophysical turbulence* (Vol. 50, pp. 225–244). Elsevier. https://doi.org/10.1016/S0422-9894(08)70443-0

Chan, J. C. L. (2005). The physics of tropical cyclone motion. *Annual Review of Fluid Mechanics*, *37*(1), 99–128. https://doi.org/10.1146/annurev.fluid.37.061903.175702

Chan, J. C. L., & Williams, R. T. (1987). Analytical and numerical studies of the beta-effect in tropical cyclone motion. Part I: Zero mean flow. *Journal of the Atmospheric Sciences*, *44*(9), 1257–1265. https://doi.org/10.1175/1520-0469

Charney, J. G., & Stern, M. E. (1962). On the stability of internal baroclinic jets in a rotating atmosphere. *Journal of the Atmospheric Sciences*, *19*(2), 159–172. https://doi.org/10.1175/1520-0469(1962)019<0159:OTSOIB>2.0.CO;2

Choi, D. S., Showman, A. P., & Brown, R. H. (2009). Cloud features and zonal wind measurements of Saturn's atmosphere as observed by Cassini/VIMS. *Journal of Geophysical Research*, *114*(E4), E04007. https://doi.org/10.1029/2008JE003254

de Pater, I., Wong, M. H., Marcus, P. S., Luszcz-Cook, S., Ádámkovics, M., Conrad, A., et al. (2010). Persistent rings in and around Jupiter's anticyclones—Observations and theory. *Icarus*, *210*(2), 742–762. https://doi.org/10.1016/j.icarus.2010.07.027

Del Genio, A. D., Achterberg, R. K., Baines, K. H., Flasar, F. M., Read, P. L., Sánchez-Lavega, A., & Showman, A. P. (2009). Saturn atmospheric structure and dynamics. In M. K. Dougherty, L. W. Esposito, & S. M. Krimigis (Eds.), *Saturn after cassini–huygens* (pp. 113–159). Springer-Verlag. https://doi.org/10.1007/978-1-4020-9217-6_5

del Río-Gaztelurrutia, T., Hueso, R., Sánchez-Lavega, A., Pérez-Hoyos, S., Legarreta, J., García-Melendo, E., & Sromovsky, L. (2018). A planetary-scale disturbance in a long-living three-vortex coupled system in Saturn's atmosphere. *Icarus*, *302*, 499–513. https://doi.org/10.1016/j.icarus.2017.12.030

Dowling, T. E., & Ingersoll, A. P. (1989). Jupiter's great Red Spot as a shallow water system. *Journal of the Atmospheric Sciences*, *46*(21), 3256–3278. https://doi.org/10.1175/1520-0469

Dyudina, U. A., Ingersoll, A. P., Ewald, S. P., Vasavada, A. R., West, R. A., Del Genio, A. D., et al. (2008). Dynamics of Saturn's south polar vortex. *Science*, *319*(5871), 1801. https://doi.org/10.1126/science.1153633

Emanuel, K. (2003). Tropical cyclones. *Annual Review of Earth and Planetary Sciences*, *31*(1), 75–104. https://doi.org/10.1146/annurev.earth.31.100901.141259

Emanuel, K. A. (1991). The theory of hurricanes. *Annual Review of Fluid Mechanics*, *23*(1), 179–196. https://doi.org/10.1146/annurev.fl.23.010191.001143

Erard, S., Cecconi, B., Le Sidaner, P., Rossi, A. P., Capria, M. T., Schmitt, B., et al. (2018). VESPA: A community-driven virtual observatory in planetary science. *Planetary and Space Science*, *150*, 65–85. https://doi.org/10.1016/j.pss.2017.05.013

Filacchione, G., Capaccioni, F., McCord, T. B., Coradini, A., Cerroni, P., Bellucci, G., et al. (2007). Saturn's icy satellites investigated by Cassini-VIMS: I. Full-disk properties: 350–5100 nm reflectance spectra and phase curves. *Icarus*, *186*(1), 259–290. https://doi.org/10.1016/j.icarus.2006.08.002

Fischer, G., Kurth, W. S., Gurnett, D. A., Zarka, P., Dyudina, U. A., Ingersoll, A. P., et al. (2011). A giant thunderstorm on Saturn. *Nature*, *475*(7354), 75–77. https://doi.org/10.1038/nature10205

Fletcher, L. N., Baines, K. H., Momary, T. W., Showman, A. P., Irwin, P. G. J., Orton, G. S., et al. (2011). Saturn's tropospheric composition and clouds from Cassini/VIMS 4.6–5.1 μm nightside spectroscopy. *Icarus*, *214*(2), 510–533. https://doi.org/10.1016/j.icarus.2011.05.020

Fletcher, L. N., Hesman, B. E., Irwin, P. G. J., Baines, K. H., Momary, T. W., Sanchez-Lavega, A., et al. (2011). Thermal structure and dynamics of Saturn's northern springtime disturbance. *Science*, *332*(6036), 1413–1417. https://doi.org/10.1126/science.1204774

Fletcher, L. N., Orton, G. S., Sinclair, J. A., Guerlet, S., Read, P. L., Antuñano, A., et al. (2018). A hexagon in Saturn's northern stratosphere surrounding the emerging summertime polar vortex. *Nature Communications*, *9*(1), 3564. https://doi.org/10.1038/s41467-018-06017-3

Flierl, G. R. (1988). On the instability of geostrophic vortices. *Journal of Fluid Mechanics*, *197*, 349–388. https://doi.org/10.1017/s0022112088003283

Gaddis, L., Anderson, J., Becker, K., Becker, T., Cook, D., Edwards, K., et al. (1997). An overview of the integrated software for imaging spectrometers (ISIS). *Lunar and Planetary Science Conference*, *28*, 387.

García-Melendo, E., Hueso, R., Sánchez-Lavega, A., Legarreta, J., del Río-Gaztelurrutia, T., Pérez-Hoyos, S., & Sanz-Requena, J. F. (2013). Atmospheric dynamics of Saturn's 2010 giant storm. *Nature Geoscience*, *6*(7), 525–529. https://doi.org/10.1038/ngeo1860

García-Melendo, E., & Sánchez-Lavega, A. (2017). Shallow-water simulations of Saturn's giant storms at different latitudes. *Icarus*, *286*, 241–260. https://doi.org/10.1016/j.icarus.2016.10.025

García-Melendo, E., Sánchez-Lavega, A., & Hueso, R. (2007). Numerical models of Saturn's long-lived anticyclones. *Icarus*, *191*, 665–677. https://doi.org/10.1016/j.icarus.2007.06.022

Gent, P. R., & McWilliams, J. C. (1986). The instability of barotropic circular vortices. *Geophysical & Astrophysical Fluid Dynamics*, *35*(1–4), 209–233. https://doi.org/10.1080/03091928608210064

Hassanzadeh, P., Marcus, P. S., & Le Gal, P. (2012). The universal aspect ratio of vortices in rotating stratified flows: Theory and simulation. *Journal of Fluid Mechanics*, *706*, 46–57. https://doi.org/10.1017/jfm.2012.198

Held, I. M., & Hou, A. Y. (1980). Nonlinear axially symmetric circulations in a nearly inviscid atmosphere. *Journal of the Atmospheric Sciences*, *37*(3), 515–533. https://doi.org/10.1175/1520-0469

Holland, G. J. (1983). Tropical cyclone motion: Environmental interaction plus a beta effect. *Journal of the Atmospheric Sciences*, *40*(2), 328–342. https://doi.org/10.1175/1520-0469(1983)040<0328:TCMEIP>2.0.CO;2

Holland, G. J. (1984). Tropical cyclone motion. A comparison of theory and observation. *Journal of the Atmospheric Sciences*, *41*(1), 68–75. https://doi.org/10.1175/1520-0469(1984)041<0068:tcmaco>2.0.co;2

Holton, J. R., & Hakim, G. J. (2013). *An introduction to dynamic meteorology* (5th ed., Vol. 88). Academic Press.

Hoskins, B. J., & Hodges, K. I. (2002). New perspectives on the Northern Hemisphere winter storm tracks. *Journal of the Atmospheric Sciences*, *59*(6), 1041–1061. https://doi.org/10.1175/1520-0469

Hueso, R., Sánchez-Lavega, A., Rojas, J. F., Simon, A. A., Barry, T., del Río-Gaztelurrutia, T., et al. (2020). Saturn atmospheric dynamics one year after Cassini: Long-lived features and time variations in the drift of the Hexagon. *Icarus*, *336*, 113429. https://doi.org/10.1016/j.icarus.2019.113429

Ingersoll, A. P., Dowling, T. E., Gierasch, P. J., Orton, G. S., Read, P. L., Sánchez-Lavega, A., et al. (2004). Dynamics of Jupiter's atmosphere. In F. Bagenal, T. E. Dowling, & W. B. McKinnon (Eds.), *Jupiter: The planet, satellites and magnetosphere* (pp. 105–128). Cambridge University Press.

Jaffe, L. D., & Herrell, L. M. (1997). Cassini/Huygens science instruments, spacecraft, and mission. *Journal of Spacecraft and Rockets*, *34*(4), 509–521. https://doi.org/10.2514/2.3264

Kimble, R. A., MacKenty, J. W., O'Connell, R. W., & Townsend, J. A. (2008). Wide Field Camera 3: A powerful new imager for the Hubble Space Telescope. In *Space telescopes and instrumentation 2008: Optical, infrared, and millimeter* (Vol. 7010, p. 70101E). International Society for Optics and Photonics (SPIE). https://doi.org/10.1117/12.789581

Kloosterziel, R. C., & Van Heijst, G. J. F. (1991). An experimental study of unstable barotropic vortices in a rotating fluid. *Journal of Fluid Mechanics*, *223*, 1–24. https://doi.org/10.1017/S0022112091001301

Knowles, B., West, R., Helfenstein, P., Verbiscer, A., Wilson, D., & Porco, C. (2020). End-of-mission calibration of the cassini imaging science subsystem. *Planetary and Space Science*, *185*, 104898. https://doi.org/10.1016/j.pss.2020.104898

Li, L., Guan, L., Li, S., Luu, C., Heng, K., Fry, P. M., et al. (2023). The bolometric Bond albedo of Enceladus. *Icarus*, *394*, 115429. https://doi.org/10.1016/j.icarus.2023.115429

Li, L., Ingersoll, A. P., Vasavada, A. R., Porco, C. C., Del Genio, A. D., & Ewald, S. P. (2004). Life cycles of spots on Jupiter from Cassini images. *Icarus*, *172*(1), 9–23. https://doi.org/10.1016/j.icarus.2003.10.015

Li, L., Ingersoll, A. P., Vasavada, A. R., Simon-Miller, A. A., Del Genio, A. D., Ewald, S. P., et al. (2006). Vertical wind shear on Jupiter from Cassini images. *Journal of Geophysical Research*, *111*(E4), E04004. https://doi.org/10.1029/2005JE002556

Li, L., Jiang, X., Ingersoll, A. P., Del Genio, A. D., Porco, C. C., West, R. A., et al. (2011). Equatorial winds on Saturn and the stratospheric oscillation. *Nature Geoscience*, *4*(11), 750–752. https://doi.org/10.1038/ngeo1292

Li, L., Jiang, X., West, R. A., Gierasch, P. J., Perez-Hoyos, S., Sánchez-Lavega, A., et al. (2018). Less absorbed solar energy and more internal heat for Jupiter. *Nature Communications*, *9*(1), 3709. https://doi.org/10.1038/s41467-018-06107-2

Li, L., Studwell, A., Dowling, T. E., Bradley, M. E., Creecy, E. C., Albright, R. J., & Jiang, X. (2021). Unsymmetrical expansion of bright clouds from Saturn's 2010 great white storm. *Icarus*, *369*, 114650. https://doi.org/10.1016/j.icarus.2021.114650

Li, X., & Wang, B. (1992). The beta drift of three-dimensional vortices: A numerical study. *Monthly Weather Review*, *120*(4), 579–593. https://doi.org/10.1175/1520-0493

Marcus, P. S. (1993). Jupiter's Great Red Spot and other vortices. *Annual Review of Astronomy and Astrophysics*, *31*(1), 523–573. https://doi.org/10.1146/annurev.aa.31.090193.002515

Marinelli, M., & Green, J. (2024). *Wide Field Camera 3 Instrument Handbook, Version 17.0*. STScI. Retrieved from https://hst-docs.stsci.edu/wfc3ihb

McWilliams, J. C., & Flierl, G. R. (1979). On the evolution of isolated, nonlinear vortices. *Journal of Physical Oceanography*, *9*(6), 1155–1182. https://doi.org/10.1175/1520-0485(1979)009<1155:OTEOIN>2.0.CO;2

Oliva, F., Adriani, A., Moriconi, M. L., Liberti, G. L., D'Aversa, E., & Filacchione, G. (2016). Clouds and hazes vertical structure of a Saturn's giant vortex from Cassini/VIMS-V data analysis. *Icarus*, *278*, 215–237. https://doi.org/10.1016/j.icarus.2016.06.008

Pedlosky, J. (1987). *Geophysical fluid dynamics*. Springer-Verlag.

Pérez-Hoyos, S., Sánchez-Lavega, A., French, R. G., & Rojas, J. F. (2005). Saturn's cloud structure and temporal evolution from ten years of Hubble Space Telescope images (1994–2003). *Icarus*, *176*(1), 155–174. https://doi.org/10.1016/j.icarus.2005.01.013

Pérez-Hoyos, S., Sanz-Requena, J. F., Sánchez-Lavega, A., & Irwin, P. G. J. (2016). Saturn's tropospheric particle phase function and spatial distribution from Cassini ISS 2011 observations. *Icarus*, *277*, 1–18. https://doi.org/10.1016/j.icarus.2016.04.037

Polvani, L. M., Zabusky, N. J., & Flierl, G. R. (1989). Two-layer geostrophic vortex dynamics. Part 1. Upper-layer v-states and merger. *Journal of Fluid Mechanics*, *205*, 215–242. https://doi.org/10.1017/S0022112089002013

Porco, C. C., Baker, E., Barbara, J., Beurle, K., Brahic, A., Burns, J. A., et al. (2005). Cassini Imaging Science: Initial results on Saturn's atmosphere. *Science*, *307*(5713), 1243–1247. https://doi.org/10.1126/science.1107691

Porco, C. C., & Cassini Imaging Science Team. (2020). ISS observations from the Cassini tour of the Saturn system. In *NASA planetary data System, urn:nasa:pds:cassini_iss_saturn::1.0*. https://doi.org/10.17189/1504133

Porco, C. C., West, R. A., Squyres, S., McEwen, A., Thomas, P., Murray, C. D., et al. (2004). Cassini imaging science: Instrument characteristics and anticipated scientific investigations at Saturn [Dataset]. *Space Science Reviews*, *115*(1–4), 363–497. https://doi.org/10.1007/s11214-004-1456-7

Read, P. L., Conrath, B., Fletcher, L., Gierasch, P., Simon-Miller, A., & Zuchowski, L. (2009). Mapping potential vorticity dynamics on Saturn: Zonal mean circulation from Cassini and Voyager data. *Planetary and Space Science*, *57*(14–15), 1682–1698. https://doi.org/10.1016/j.pss.2009.03.004

Read, P. L., Dowling, T. E., & Schubert, G. (2009). Saturn's rotation period from its atmospheric planetary-wave configuration. *Nature*, *460*(7255), 608–610. https://doi.org/10.1038/nature08194

Ripa, P. (1987). On the stability of elliptical vortex solutions of the shallow-water equations. *Journal of Fluid Mechanics*, *183*, 343–363. https://doi.org/10.1017/s0022112087002660

Roman, M. T., Banfield, D., & Gierasch, P. J. (2013). Saturn's cloud structure inferred from Cassini ISS. *Icarus*, *225*(1), 93–110. https://doi.org/10.1016/j.icarus.2013.03.014

Rossby, C.-G. (1948). On displacements and intensity changes of atmospheric vortices. *Journal of Marine Research*, *7*, 175–187.

Sánchez-Lavega, A., del Río-Gaztelurrutia, T., Delcroix, M., Legarreta, J. J., Gómez-Forrellad, J. M., Hueso, R., et al. (2012). Ground-based observations of the long-term evolution and death of Saturn's 2010 Great White Spot. *Icarus*, *220*, 561–576. https://doi.org/10.1016/j.icarus.2012.05.022

Salby, M. L. (1996). *Fundamentals of atmospheric physics*. Academic Press.

Sánchez-Lavega, A., del Río-Gaztelurrutia, T., Hueso, R., Gómez-Forrellad, J. M., Sanz-Requena, J. F., Legarreta, J., et al. (2011). Deep winds beneath Saturn's upper clouds from a long-lived planetary-scale storm. *Nature*, *475*(7354), 71–74. https://doi.org/10.1038/nature10203

Sánchez-Lavega, A., García-Melendo, E., Legarreta, J., Miró, A., Soria, M., & Ahrens-Velásquez, K. (2024). The origin of Jupiter's Great Red Spot. *Geophysical Research Letters*, *51*(12), e2024GL108993. https://doi.org/10.1029/2024GL108993

Sánchez-Lavega, A., Hueso, R., & Pérez-Hoyos, S. (2007). The three-dimensional structure of Saturn's equatorial jet at cloud level. *Icarus*, *187*(2), 510–519. https://doi.org/10.1016/j.icarus.2006.10.022

Sánchez-Lavega, A., Hueso, R., Pérez-Hoyos, S., & Rojas, J. F. (2006). A strong vortex in Saturn's South Pole. *Icarus*, *184*(2), 524–531. https://doi.org/10.1016/j.icarus.2006.05.020

Sánchez-Lavega, A., Lecacheux, J., Colas, F., & Laques, P. (1993). Ground-based observations of Saturn's North Polar Spot and hexagon. *Science*, *260*(5106), 329–332. https://doi.org/10.1126/science.260.5106.329

Sánchez-Lavega, A., Legarreta, J., García-Melendo, E., Hueso, R., Pérez-Hoyos, S., Gómez-Forrellad, J. M., et al. (2013). Colors of Jupiter's large anticyclones and the interaction of a tropical red oval with the Great Red Spot in 2008. *Journal of Geophysical Research: Planets*, *118*, 1–21. https://doi.org/10.1002/jgre.20018

Sánchez-Lavega, A., Rojas, J. F., Acarreta, J. R., Lecacheux, J., Colas, F., & Sada, P. V. (1997). New observations and studies of Saturn's long-lived North Polar Spot. *Icarus*, *128*, 322–334. https://doi.org/10.1006/icar.1997.5732

Sanz-Requena, J. F., Pérez-Hoyos, S., Sánchez-Lavega, A., del Río-Gaztelurrutia, T., Irwin, P. G. J., & Sromovsky, L. A. (2019). Hazes and clouds in a singular triple vortex in Saturn's atmosphere from HST/WFC3 multispectral imaging. *Icarus*, *333*, 22–36. https://doi.org/10.1016/j.icarus.2019.05.004

Sayanagi, K. M., Baines, K. H., Dyudina, U., Fletcher, L. N., Sánchez-Lavega, A., & West, R. A. (2018). Saturn's polar atmosphere. In *Saturn in the 21st century*. Cambridge University Press. https://doi.org/10.1017/9781316227220.012

Sayanagi, K. M., Dyudina, U. A., Ewald, S. P., Fischer, G., Ingersoll, A. P., Kurth, W. S., et al. (2013). Dynamics of Saturn's great storm of 2010–2011 from Cassini ISS and RPWS. *Icarus*, *223*(1), 460–478. https://doi.org/10.1016/j.icarus.2012.12.013

Simon, A. (2015). Outer Planet Atmospheres Legacy ("OPAL"), MAST archive at Space Telescope Science Institute. https://doi.org/10.17909/T9G593

Simon, A. A., Hueso, R., Sánchez-Lavega, A., & Wong, M. H. (2021). Midsummer atmospheric changes in Saturn's northern hemisphere from the Hubble OPAL program. *The Planetary Science Journal*, *2*(2), 47. https://doi.org/10.3847/psj/abe40f

Simon, A. A., Tabataba-Vakili, F., Cosentino, R., Beebe, R. F., Wong, M. H., & Orton, G. S. (2018). Historical and contemporary trends in the size, drift, and color of Jupiter's Great Red Spot. *The Astronomical Journal*, *155*(4), 151. https://doi.org/10.3847/1538-3881/aaae01

Simon, A. A., Wong, M. H., & Orton, G. S. (2015). First results from the Hubble OPAL program: Jupiter in 2015. *The Astrophysical Journal*, *812*(1), 55. https://doi.org/10.1088/0004-637X/812/1/55

Simon, A. A., Wong, M. H., Sromovsky, L. A., Fletcher, L. N., & Fry, P. M. (2022). Giant planet atmospheres: Dynamics and variability from UV to Near-IR hubble and adaptive optics imaging. *Remote Sensing*, *14*(6), 1518. https://doi.org/10.3390/rs14061518

Smith, R. B. (1993). A hurricane beta-drift law. *Journal of the Atmospheric Sciences*, *50*(18), 3213–3215. https://doi.org/10.1175/1520-0469(1993)050<3213:AHBDL>2.0.CO;2

Smith, R. B., Li, X., & Wang, B. (1997). Scaling laws for barotropic vortex beta-drift. *Tellus A*, *49*(4), 474–485. https://doi.org/10.3402/tellusa.v49i4.14684

Sromovsky, L. A., Fry, P. M., & Baines, K. H. (2002). The unusual dynamics of northern dark spots on Neptune. *Icarus*, *156*(1), 16–36. https://doi.org/10.1006/icar.2001.6761

Sromovsky, L. A., Baines, K. H., & Fry, P. M. (2013). Saturn's Great storm of 2010–2011: Evidence for ammonia and water ices from analysis of VIMS spectra. *Icarus*, *226*(1), 402–418. https://doi.org/10.1016/j.icarus.2013.05.043

Sromovsky, L. A., Baines, K. H., & Fry, P. M. (2021). Evolution of Saturn's north polar color and cloud structure between 2012 and 2017 inferred from Cassini VIMS and ISS observations. *Icarus*, *362*, 114409. https://doi.org/10.1016/j.icarus.2021.114409

Sromovsky, L. A., Baines, K. H., Fry, P. M., & Momary, T. W. (2016). Cloud clearing in the wake of Saturn's Great Storm of 2010–2011 and suggested new constraints on Saturn's He/H_2 ratio. *Icarus*, *276*, 141–162. https://doi.org/10.1016/j.icarus.2016.04.003

Sromovsky, L. A., & Fry, P. M. (2010). The source of widespread 3-μm absorption in Jupiter's clouds: Constraints from 2000 Cassini VIMS observations. *Icarus*, *210*(1), 230–257. https://doi.org/10.1016/j.icarus.2010.06.039

Sromovsky, L. A., Fry, P. M., Dowling, T. E., Baines, K. H., & Limaye, S. S. (2001). Neptune's atmospheric circulation and cloud morphology: Changes revealed by 1998 HST imaging. *Icarus*, *150*(2), 244–260. https://doi.org/10.1006/icar.2000.6574

Trammell, H. J., Li, L., Jiang, X., Pan, Y., Smith, M. A., Bering, E. A., III, et al. (2016). Vortices in Saturn's northern hemisphere (2008–2015) observed by Cassini ISS. *Journal of Geophysical Research: Planets*, *121*(9), 1814–1826. https://doi.org/10.1002/2016JE005122

Trammell, H. J., Li, L., Jiang, X., Smith, M., Hörst, S., & Vasavada, A. (2014). The global vortex analysis of Jupiter and Saturn based on Cassini Imaging Science Subsystem. *Icarus*, *242*, 122–129. https://doi.org/10.1016/j.icarus.2014.08.022

Vasavada, A. R., Hörst, S. M., Kennedy, M. R., Ingersoll, A. P., Porco, C. C., Del Genio, A. D., & West, R. A. (2006). Cassini imaging of Saturn: Southern hemisphere winds and vortices. *Journal of Geophysical Research*, *111*(E5), E05004. https://doi.org/10.1029/2005JE002563

Wallace, J. M., & Hobbs, P. V. (2006). *Atmospheric science: An introductory survey* (Vol. 92). Elsevier.

Wang, X. (2026). A long-lived vortex from saturn's 2010 giant convective storm [Dataset]. *Zenodo*. https://doi.org/10.5281/zenodo.18985853

Wang, X., Li, L., Guan, L., Jiang, X., Fry, P. M., Dyudina, U. A., et al. (2025). Spatiotemporal variability of Saturn's zonal winds observed by Cassini. *Journal of Geophysical Research: Planets*, *130*(1), e2024JE008515. https://doi.org/10.1029/2024JE008515

Wang, Y., & Li, Y. (1996). Dynamics of Baroclinic vortex drift in a stratified atmosphere. *Journal of the Atmospheric Sciences*, *53*, 3307–3322. https://doi.org/10.1175/1520-0469(1996)053<3307:DOBVDI>2.0.CO;2

Waugh, D. W., & Randel, W. J. (1999). Climatology of Arctic and Antarctic polar vortices using elliptical diagnostics. *Journal of the Atmospheric Sciences*, *56*(11), 1594–1613. https://doi.org/10.1175/1520-0469

West, R., Knowles, B., Birath, E., Charnoz, S., Di Nino, D., Hedman, M., et al. (2010). In-flight calibration of the Cassini imaging science subsystem cameras. *Planetary and Space Science*, *58*(11), 1475–1488. https://doi.org/10.1016/j.pss.2010.07.006

West, R. A., Baines, K. H., Karkoschka, E., & Sánchez-Lavega, A. (2009). Clouds and aerosols in Saturn's atmosphere. In M. K. Dougherty, L. W. Esposito, & S. M. Krimigis (Eds.), *Saturn from cassini-huygens* (pp. 161–179). Springer. https://doi.org/10.1007/978-1-4020-9217-6_7

Wong, M. H., de Pater, I., Asay-Davis, X., Marcus, P. S., & Go, C. Y. (2011). Vertical structure of Jupiter's Oval BA before and after it reddened: What changed? *Icarus*, *215*(1), 211–225. https://doi.org/10.1016/j.icarus.2011.06.032

Wong, M. H., Hsu, A. I., & Simon, A. A. (2019). Lifetimes and occurrence rates of dark vortices on Neptune from 25 years of Hubble Space Telescope images. *The Astronomical Journal*, *157*(3), 117. https://doi.org/10.3847/1538-3881/ab0747

Wong, M. H., Marcus, P. S., Simon, A. A., de Pater, I., Tollefson, J. W., & Asay-Davis, X. (2021). Evolution of the horizontal winds in Jupiter's great red spot from one Jovian year of HST/WFC3 maps. *Geophysical Research Letters*, *48*(18), e93982. https://doi.org/10.1029/2021GL093982

Wong, M. H., Sromovsky, L. A., Fry, P. M., Sánchez-Lavega, A., Hueso, R., Legarreta, J., et al. (2022). Evolution of a dark vortex on Neptune with transient secondary features. *Icarus*, *387*, 115123. https://doi.org/10.1016/j.icarus.2022.115123

Wong, M. H., Tollefson, J., Hsu, A. I., de Pater, I., Simon, A. A., Hueso, R., et al. (2018). A new dark vortex on Neptune. *The Astronomical Journal*, *155*(3), 117. https://doi.org/10.3847/1538-3881/aaa6d6